

# Healable and conductive sulfur iodide for solid-state Li–S batteries

<https://doi.org/10.1038/s41586-024-07101-z>

Received: 4 September 2023

Accepted: 22 January 2024

Published online: 06 March 2024

 Check for updates

Jianbin Zhou<sup>1,11</sup>, Manas Likhit Holekevi Chandrappa<sup>1,11</sup>, Sha Tan<sup>2</sup>, Shen Wang<sup>1</sup>, Chaoshan Wu<sup>3</sup>, Howie Nguyen<sup>4</sup>, Canhui Wang<sup>5</sup>, Haodong Liu<sup>1</sup>, Sicen Yu<sup>1</sup>, Quin R. S. Miller<sup>6</sup>, Gayea Hyun<sup>1</sup>, John Holoubek<sup>1</sup>, Junghwa Hong<sup>1</sup>, Yuxuan Xiao<sup>7</sup>, Charles Soulé<sup>1</sup>, Zheng Fan<sup>8</sup>, Eric E. Fullerton<sup>7</sup>, Christopher J. Brooks<sup>9</sup>, Chao Wang<sup>5</sup>, Raphaële J. Clément<sup>4</sup>, Yan Yao<sup>3</sup>, Enyuan Hu<sup>2</sup>, Shyue Ping Ong<sup>1,10</sup> & Ping Liu<sup>1,10</sup>

Solid-state Li–S batteries (SSLSBs) are made of low-cost and abundant materials free of supply chain concerns. Owing to their high theoretical energy densities, they are highly desirable for electric vehicles<sup>1–3</sup>. However, the development of SSLSBs has been historically plagued by the insulating nature of sulfur<sup>4,5</sup> and the poor interfacial contacts induced by its large volume change during cycling<sup>6,7</sup>, impeding charge transfer among different solid components. Here we report an  $\text{S}_{9,3}\text{I}$  molecular crystal with  $\text{I}_2$  inserted in the crystalline sulfur structure, which shows a semiconductor-level electrical conductivity (approximately  $5.9 \times 10^{-7} \text{ S cm}^{-1}$ ) at 25 °C; an 11-order-of-magnitude increase over sulfur itself. Iodine introduces new states into the band gap of sulfur and promotes the formation of reactive polysulfides during electrochemical cycling. Further, the material features a low melting point of around 65 °C, which enables repairing of damaged interfaces due to cycling by periodical remelting of the cathode material. As a result, an  $\text{Li}-\text{S}_{9,3}\text{I}$  battery demonstrates 400 stable cycles with a specific capacity retention of 87%. The design of this conductive, low-melting-point sulfur iodide material represents a substantial advancement in the chemistry of sulfur materials, and opens the door to the practical realization of SSLSBs.

Solid-state Li–S batteries (SSLSBs) with inorganic solid electrolytes do not suffer from the capacity fade associated with the ‘polysulfide shuttle’ phenomenon in liquid electrolytes<sup>8,9</sup>. They involve direct conversion between S and  $\text{Li}_2\text{S}$  during cycling<sup>4,10</sup>, and rely entirely on the interfaces between the solid electrolytes, conductive carbon and S species to transfer charge<sup>11,12</sup>. This reliance paired with the insulating nature of S (electrical conductivity of approximately  $5 \times 10^{-18} \text{ S cm}^{-1}$ ) is untenable. Further, S expands by around 79% when converted to  $\text{Li}_2\text{S}$ , leading to failures of solid/solid interfaces (Extended Data Fig. 1a)<sup>13,14</sup>. By contrast, a liquid/solid interface always maintains perfect contact. In this regard, a sulfur material with intrinsic conductivity and a low melting point will allow for the initial formation and subsequent re-formation of perfect interfaces (Extended Data Fig. 1b).

$\text{S}_{9,3}\text{I}$  is readily synthesized by grinding stoichiometric amounts of S and  $\text{I}_2$  powder in air and heating the mixture to 80 °C in a sealed container (Extended Data Fig. 1c). The melting point of  $\text{S}_{9,3}\text{I}$  is approximately 65 °C as confirmed by differential scanning calorimetry (DSC; Extended Data Fig. 1d) and in situ X-ray diffraction (XRD; Extended Data Fig. 1e). Scanning electron microscopy (SEM) combined with energy-dispersive X-ray spectroscopy (EDX) mapping (Extended Data Fig. 1g–i) indicates that the as-prepared  $\text{S}_{9,3}\text{I}$  solid has a homogeneous

distribution of S and I.  $\text{S}_{9,3}\text{I}$  seems to be a unique composition on the basis of DSC analysis, where residual S or  $\text{I}_2$  is observed except for the 9.3:1 ratio. These results are also consistent with the Raman spectra (Extended Data Fig. 1f).

The XRD pattern of  $\text{S}_{9,3}\text{I}$  (Fig. 1a) seems to be very similar to that of S in the wide-angle region, but has a prominent broad peak centred at approximately 1.5°. This peak corresponds to a d-spacing of 5.8 nm, indicative of the formation of a superstructure. More information on the XRD analysis can be found in Extended Data Fig. 1j. Atomic pair distribution function (PDF) analysis (Fig. 1b) shows an absence of  $\text{I}_2$  with long range ordering, but I–I remains after melting. In S PDF, the peaks at around 2.0 Å, 3.3 Å and 4.5 Å correspond to unique correlations within the  $\text{S}_8$  puckered ring. Their dominance along with the presence of the 2.7 Å peak in the  $\text{S}_{9,3}\text{I}$  PDF indicate the structure is mainly composed of  $\text{S}_8$  rings with the insertion of  $\text{I}_2$  molecules. The mass spectra of  $\text{S}_{9,3}\text{I}$  and S further show that  $\text{I}_2$  molecules are inserted into the S structure (Extended Data Fig. 1k). Further PDF analyses of sulfur iodide with different S:I ratios (Extended Data Fig. 1l) are consistent with the DSC, XRD and Raman data. Moreover, solid  $\text{S}_{9,3}\text{I}$  has a density of  $2.45 \text{ g cm}^{-3}$ , slightly higher than that of sulfur ( $2.07 \text{ g cm}^{-3}$ ). The material density remains rather constant in its liquid (approximately  $2.35 \text{ g cm}^{-3}$ ) and

<sup>1</sup>Department of Nanoengineering, University of California, San Diego, La Jolla, CA, USA. <sup>2</sup>Chemistry Division, Brookhaven National Laboratory, Upton, NY, USA. <sup>3</sup>Materials Science and Engineering Program and Texas Center for Superconductivity at the University of Houston, University of Houston, Houston, TX, USA. <sup>4</sup>Materials Department and Materials Research Laboratory, University of California, Santa Barbara, CA, USA. <sup>5</sup>Department of Chemical and Biomolecular Engineering, Johns Hopkins University, Baltimore, MD, USA. <sup>6</sup>Energy and Environment Directorate, Pacific Northwest National Laboratory, Richland, WA, USA. <sup>7</sup>Center for Memory and Recording Research, University of California, La Jolla, San Diego, CA, USA. <sup>8</sup>Department of Engineering Technology, University of Houston, Houston, TX, USA. <sup>9</sup>Honda Research Institute USA, 99P Labs, Columbus, OH, USA. <sup>10</sup>Sustainable Power and Energy Center, University of California, San Diego, La Jolla, CA, USA. <sup>11</sup>These authors contributed equally: Jianbin Zhou, Manas Likhit Holekevi Chandrappa. <sup>✉</sup>e-mail: ongsp@ucsd.edu; piliu@ucsd.edu

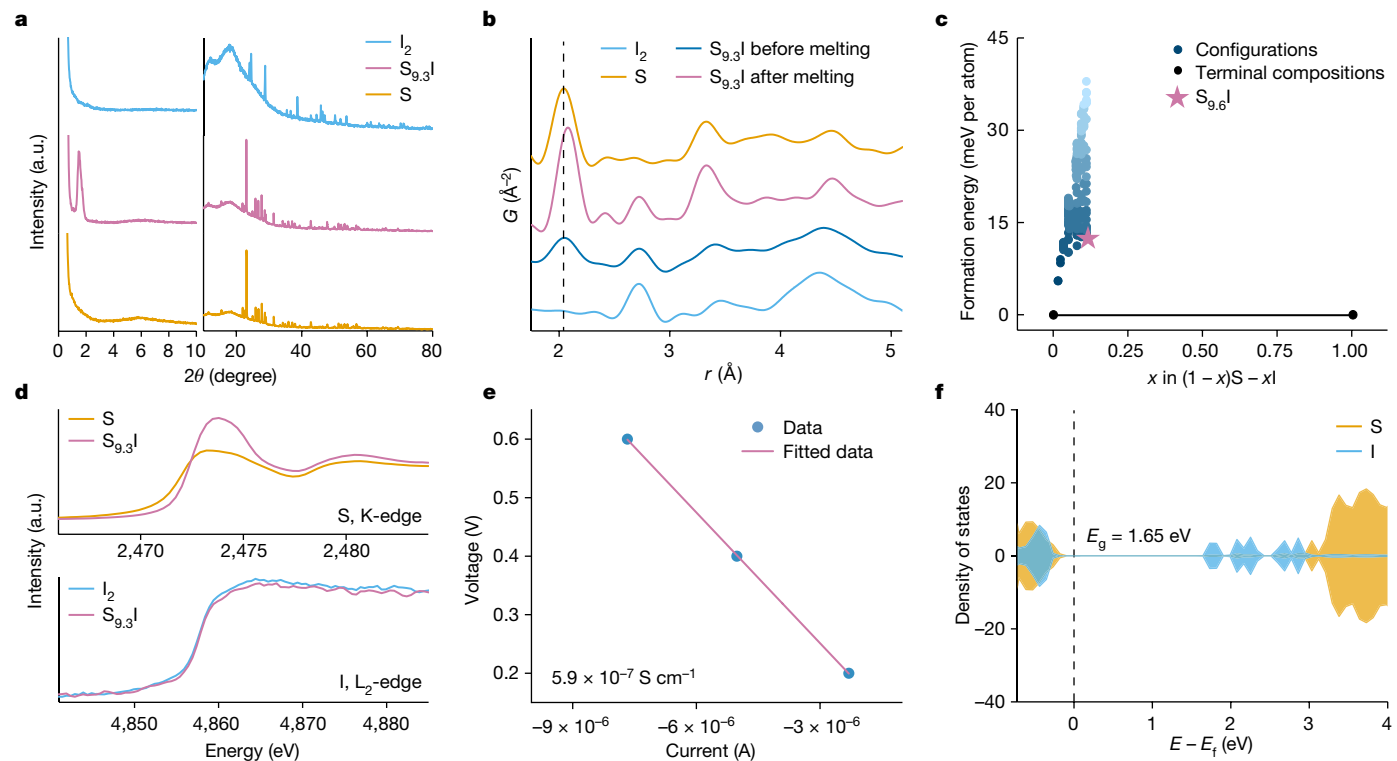


**Fig. 1 | Structure and property characterizations of  $S_{9.3}I$ .** **a**, XRD ( $K\alpha$   $\lambda = 1.5418 \text{ \AA}$ ) of  $S$ ,  $S_{9.3}I$  and  $I_2$ . **b**, PDF analysis of  $S$ ,  $I_2$  and  $S_{9.3}I$  before and after initial melting. **c**, The pseudo-binary  $S$ – $I$  phase diagram. **d**,  $S$  K-edge and  $I$   $L_2$ -edge XAS data of elemental  $S$ ,  $I_2$  and  $S_{9.3}I$ . **e**, Electrical conductivity of  $S_{9.3}I$  at

25 °C, measured by the equilibrium current versus applied voltages. **f**, Elemental projected density of states for  $S_{9.6}I$  from HSE calculations. a.u., arbitrary units;  $E$ , energy;  $E_f$ , Fermi level;  $E_g$ , band gap;  $G$ , pair distribution function;  $r$ , distance.

solid states, essential for using the remelting method to repair microstructural damages.

To elucidate the structure of  $S_{9.3}I$ , density functional theory (DFT) calculations are performed by using the Strongly Constrained and Appropriately Normed (SCAN) meta-GGA functional. The SCAN functional yields better agreement with experimental cell parameters for  $S$  (Extended Data Table 1) and has been extensively benchmarked on the energetics and structure relaxations of diversely bonded materials<sup>15</sup>. The calculations were performed on candidate structures wherein  $S_8$  rings (molecular mass = 256.48 g mol<sup>-1</sup>) within orthorhombic octasulfur are substituted by linear  $I_2$  (253.8 g mol<sup>-1</sup>) or  $I_3$  (380.7 g mol<sup>-1</sup>) molecules, spanning a compositional range from  $S_{60}I$  (one  $I_2$  substituting for a single  $S_8$  unit in the octasulfur unit cell) to  $S_8I$  (six  $I_2$  replacing four  $S_8$  units). We find that the lowest energy configuration of the  $S_{9.3}I$  composition (five  $I_2$  replacing four  $S_8$  units) is close to the experimental  $S_{9.3}I$  composition, and has a small energy above hull of 13 meV per atom (Fig. 1c). It is well within the typical energy range of thermal contributions at room temperature (around 25 meV per atom) and typical thresholds of energies above hull used to ascertain potential synthesizability of materials (around 50 meV per atom)<sup>16</sup>. The relaxed  $S_{9.3}I$  configuration has a negligible 3% volume shrinkage and a higher computed density of 2.21 g cm<sup>-3</sup> compared with bulk  $S$ , which is consistent with the experimental observations. The computed XRD patterns also feature a peak at low angles, indicative of a superstructure (Extended Data Fig. 2a). The computed PDF of  $S_{9.3}I$  structure matches well with the experimental data with major peaks present at 2, 2.7 and 3.4 Å (Extended Data Fig. 2b). We also note that the SCAN lattice energy of  $S_{9.3}I$  (-361 meV per molecule) is approximately 40 meV per molecule smaller than that of  $S$  (-400 meV per molecule). This indicates that  $I_2$  incorporation disrupts the van der Waals interactions in  $S_8$ , which contributes to the lowered melting point. The structures in the  $S_{9.6}I$ – $S_8I$  compositional space are also analysed to understand the broader impact/trend of  $I_2$

substitution (Extended Data Fig. 2c). Unless specified, the results of  $S_{9.6}I$  composition hold for all these compositions.

Using Bader charge analysis, we quantified the charge transfer between  $S$  and  $I$  in  $S_{9.6}I$  by calculating the net difference between the charge on an  $I$  atom in  $S_{9.6}I$  and the number of valence electrons in atomic  $I$ . A small charge transfer of 0.067 electrons is found, indicating limited charge transfer. This is corroborated by the experimental  $S$  K-edge and  $I$   $L_2$ -edge X-ray absorption spectroscopy (XAS; Fig. 1d). Changes in electronic structure of  $S$  upon formation of  $S_{9.3}I$  are further probed by electron paramagnetic resonance (EPR). In situ EPR spectra during heating from 20 °C to 150 °C (Extended Data Fig. 3a,b) show the radical concentration in  $S_{9.3}I$  grows with increasing temperature; by contrast, no EPR signal is obtained from pure  $S$ . The high level of radicals in  $S_{9.3}I$  (Extended Data Fig. 3c) motivates us to measure its electrical conductivity, which is found to be  $5.9 \times 10^{-7} \text{ S cm}^{-1}$  at 25 °C (Fig. 1e and Extended Data Fig. 3d–f), an 11-orders-of-magnitude increase over elemental  $S$ . This observation can be rationalized by visualizing the computed partial density of states of  $S$  and  $S_{9.6}I$ . Pure  $S$  has a Heyd–Scuseria–Ernzerhof (HSE) functional band gap of 2.92 eV (Extended Data Fig. 2d), slightly higher than experimental values of 2.4–2.7 eV reported previously<sup>17,18</sup>. The introduction of  $I_2$  adds states within the gap and reduces the HSE band gap to 1.65 eV (Fig. 1f). A qualitatively similar result is obtained for the SCAN functional (Extended Data Fig. 2e,f). There is only a small overlap between the  $S$  and  $I$  states, consistent with the fact that little charge transfer is observed between  $S_8$  and  $I_2$ . We find that there is a monotonic decrease in the band gap with increasing  $I$  concentration (Extended Data Fig. 2d). We note that iodine itself has semiconducting properties due to electronic interactions between neighbouring  $I_2$  molecules, and we believe that such interactions also occur in sulfur iodides. This decrease in the band gap upon introducing  $I_2$  species into the system explains the increase in conductivity from elemental  $S$  to  $S_{9.6}I$ . Additionally, the absence of partially filled bands

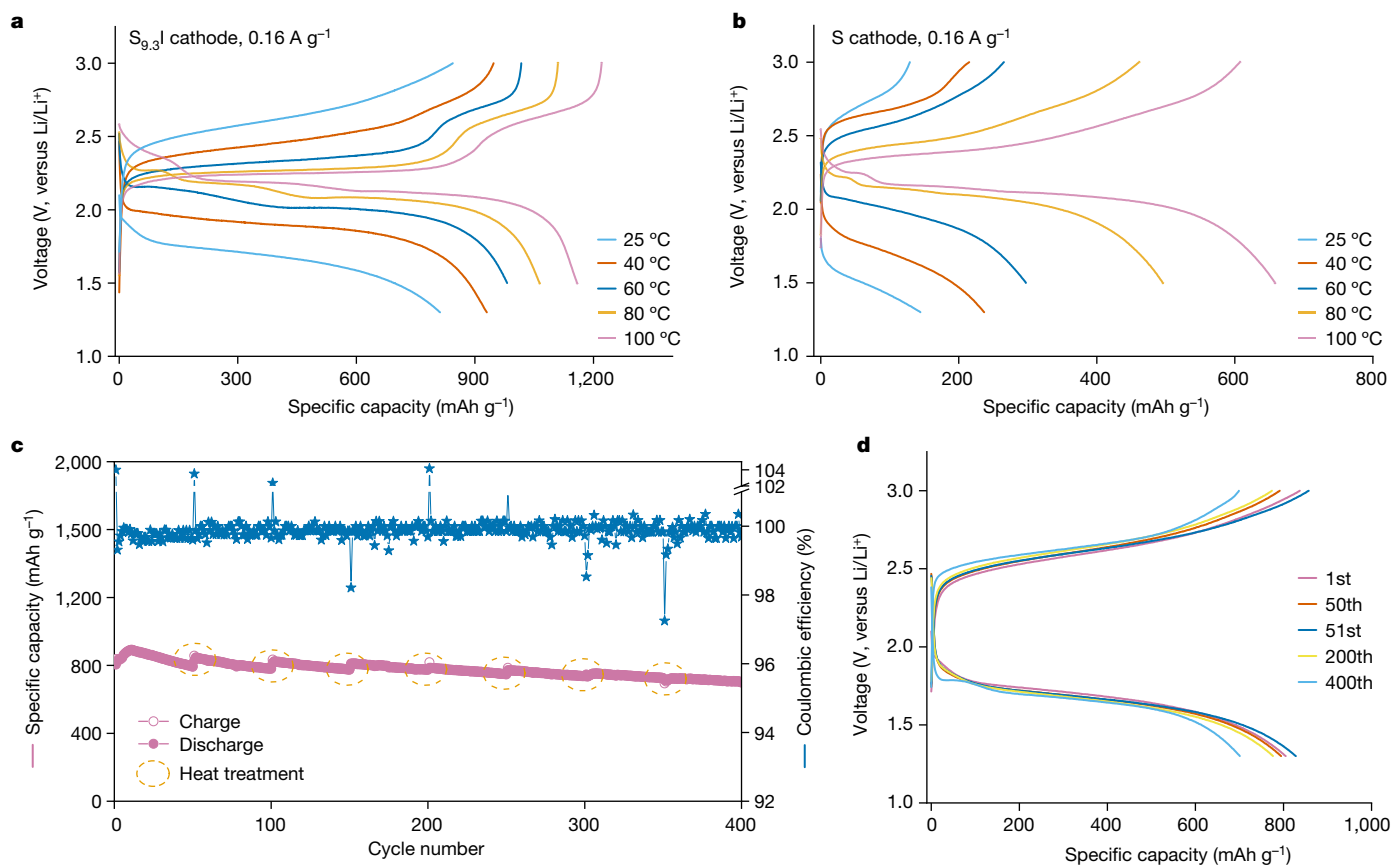


**Fig. 2 | The electrochemical performance of  $S_{9.3}I$  and elemental S cathodes in solid-state Li–S cells.** **a,b**, Discharge/charge profiles of  $S_{9.3}I$  cathode (**a**) and elemental S cathode (**b**) at  $0.16 \text{ A g}^{-1}$  from  $25^\circ\text{C}$  to  $100^\circ\text{C}$ . **c**, Long-term cycling

performance of  $S_{9.3}I$  cathode at  $0.16 \text{ A g}^{-1}$  and at  $25^\circ\text{C}$ . **d**, Corresponding voltage profiles at different cycles from **c**.

and the limited charge transfer between  $S_8$  and  $I_2$  molecules indicate that sulfur iodide is a thermodynamically metastable material rather than a dynamically stabilized one<sup>19</sup>.

$S_{9.3}I$  is evaluated in a solid-state battery with  $\text{Li}_3\text{PS}_4$  (LPS) as the electrolyte. The cathode composite is melted at  $100^\circ\text{C}$  to achieve excellent interfacial contact (Extended Data Fig. 4). LPS is chosen as it is found to contribute limited capacity (Extended Data Fig. 5a–d). Super P carbon (SP) is applied as an interlayer between Li and solid electrolyte to stop the growth of Li dendrites (Extended Data Fig. 5e,f), which is inspired by the Ag/C interlayer design reported previously<sup>20</sup>. We note that there are other promising approaches to address the Li anode stability issue<sup>21</sup>. More details are provided in the Methods.

The Li– $S_{9.3}I$  cell (Fig. 2a) is cycled at a current density of  $0.16 \text{ A g}^{-1}$  and at different temperatures. Specific capacities ranging from  $811.8$  to  $1,211.3 \text{ mAh g}^{-1}$  are delivered from  $25^\circ\text{C}$  to  $100^\circ\text{C}$ . Increasing the operating temperature greatly enhances cell kinetics as demonstrated by smaller polarization and higher capacities. The stability of the cells operating above the melting point of  $S_{9.3}I$  is enabled by its high viscosity coupled with our cell design (Methods). By contrast, the elemental S cathode (Fig. 2b) delivers much lower capacities, probably owing to its poor electronic conductivity. The differential capacity analysis profiles ( $dQ/dV$ ) of the S cathode show one redox reaction plateau (Extended Data Fig. 6a,b), whereas  $S_{9.3}I$  shows two, implying their distinct working mechanisms. The two plateaus for  $S_{9.3}I$  are most likely related to the polysulfide intermediates that are absent in the S cathode reactions.  $S_{9.3}I$  exhibits the most stable and highest capacity compared with materials with other S:I ratios (Extended Data Fig. 6c,d). Moreover, a capacity of  $489.4 \text{ mAh g}^{-1}$  is delivered even at a rate of  $5.60 \text{ A g}^{-1}$ , comparing favourably with other reported SSLSBs (Extended Data Fig. 6e–g and Extended Data Table 2)<sup>9,13,14,22–28</sup>. At a loading of  $4.2 \text{ mg cm}^{-2}$  of  $S_{9.3}I$ ,

the cathode still delivers a specific capacity of  $968.5 \text{ mAh g}^{-1}$  after 50 cycles at  $0.32 \text{ A g}^{-1}$  (Extended Data Fig. 6h,i). The anode interface is still well maintained and Li is deposited underneath the SP interlayer (Extended Data Fig. 7).

Long-term cycling performance at room temperature is critical towards the practical application of SSLSBs. When cycled at a current density of  $0.16 \text{ A g}^{-1}$  (Fig. 2c), the capacity of the  $S_{9.3}I$  cathode increases slightly owing to progressive activation during the initial 10 cycles, but decays to  $794.6 \text{ mAh g}^{-1}$  by the 50th cycle. This fade is attributed to degradation of the cathode interfaces and can be addressed by briefly remelting the cathode at  $100^\circ\text{C}$  before cycling again at  $25^\circ\text{C}$ , in which the full cell capacity recovers to  $828.1 \text{ mAh g}^{-1}$ . In this regard, the Li– $S_{9.3}I$  full cell can be periodically repaired in situ over its lifetime. By heat treating the cell every 50 cycles, a capacity of  $701 \text{ mAh g}^{-1}$  (87% retention) and an average Coulombic efficiency of about 99.8% are maintained after 400 cycles, outperforming other reported SSLSBs (Extended Data Fig. 6j and Extended Data Table 2). The voltage profiles (Fig. 2d) at different cycles indicate minimal polarization increase. Moreover,  $S_{9.3}I$  cathodes at  $40^\circ\text{C}$ ,  $60^\circ\text{C}$  and  $80^\circ\text{C}$  also show excellent Coulombic efficiency and cycling stability (Extended Data Fig. 6k–m). Electrochemical impedance spectroscopy (EIS) results confirm the enhancement in electrode kinetics for  $S_{9.3}I$  over S (Extended Data Fig. 8). The remarkable electrical conductivity and melt-driven interface repair provided by the  $S_{9.3}I$  cathode result in accelerated electrochemical reaction kinetics, solving many of the operational challenges of SSLSBs.

To probe the working mechanism of the  $S_{9.3}I$  cathode, Fig. 3a shows the S K-edge XAS of the cathode at different states of charge. The S–S  $\pi^*$  feature in  $S_8$  (ref. 29) shifts to lower energy levels, corresponding to the formation of short chain  $\text{LiS}_x$  when discharged to  $1.7 \text{ V}$  (D- $1.7 \text{ V}$ ),

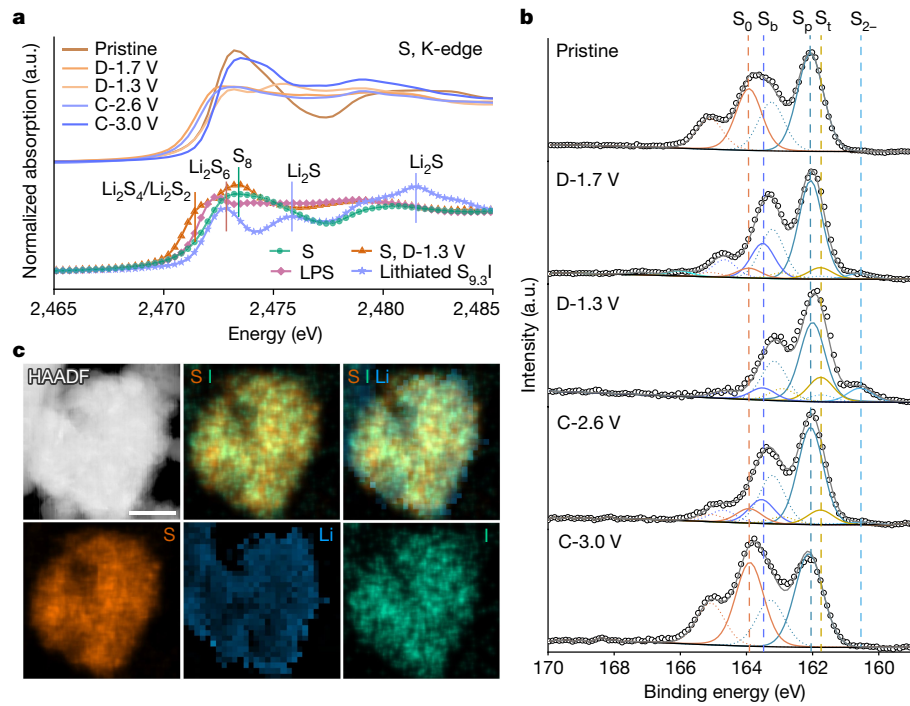


**Fig. 3 | The working mechanism of  $S_{9.3}I$  cathode in  $Li-S_{9.3}I$  cell at 25 °C.** **a**, S K-edge XAS spectra of  $S_{9.3}I$  cathode during the initial cycle. **b**,  $S_{2p}$  high resolution XPS of  $S_{9.3}I$  cathode during the initial cycle. **c**, Cryo-TEM HAADF (high-angle

annular dark-field), EDX and EELS mapping images of chemically lithiated  $S_{9.3}I$ . S and I maps are acquired by using EDX, Li map is acquired by using EELS. Scale bar, 200 nm.

and further shifts to those attributed to  $Li_2S$  and long chain  $LiS_x$  when discharged to 1.3 V (D-1.3 V). This process is fully reversible, as  $S_8$  features are recovered upon charge to 3.0 V (C-3.0 V). This reversibility is also corroborated with the  $S_{2p}$  X-ray photoelectron spectroscopy (XPS) spectra (Fig. 3b). In the pristine state, only  $S_0$  (elemental S, 163.9 eV) and  $S_p$  (LPS, 162.0 eV) signals can be resolved<sup>30</sup>. On discharge to 1.7 V, the peak intensity of  $S_0$  decreases and the peaks assigned to  $S_b$  (bridge S in  $LiS_x$ , 163.5 eV),  $S_t$  (terminal S in  $LiS_x$ , 161.7 eV) and  $S_2$  ( $Li_2S$ , 160.5 eV) increase<sup>31,32</sup>. When further discharged to 1.3 V,  $S_0$  peak disappears,  $S_b$  and  $S_t$  peaks decrease, and the  $S_2$  peak increases. XPS confirms the

good reversibility shown in the XAS data, again returning to the pristine state after charging to 3.0 V (Extended Data Fig. 9a). The excellent reversibility of the  $S_{9.3}I$  cathode is also demonstrated by ex situ Raman (Extended Data Fig. 9b) and ex situ EPR (Extended Data Fig. 9c–f).

To probe the mechanism further, a chemically lithiated  $S_{9.3}I$  prepared at an equivalent discharge capacity of approximately 800 mAh g<sup>-1</sup> (Methods) is shown to contain large amounts of long chain  $LiS_x$  along with  $Li_2S$  as indicated by XAS (Fig. 3a) and XPS (Extended Data Fig. 9g) results. By contrast, the elemental S cathode discharged to 1.3 V shows negligible amounts of  $LiS_x$  and a small amount of  $Li_2S$ . The existence of

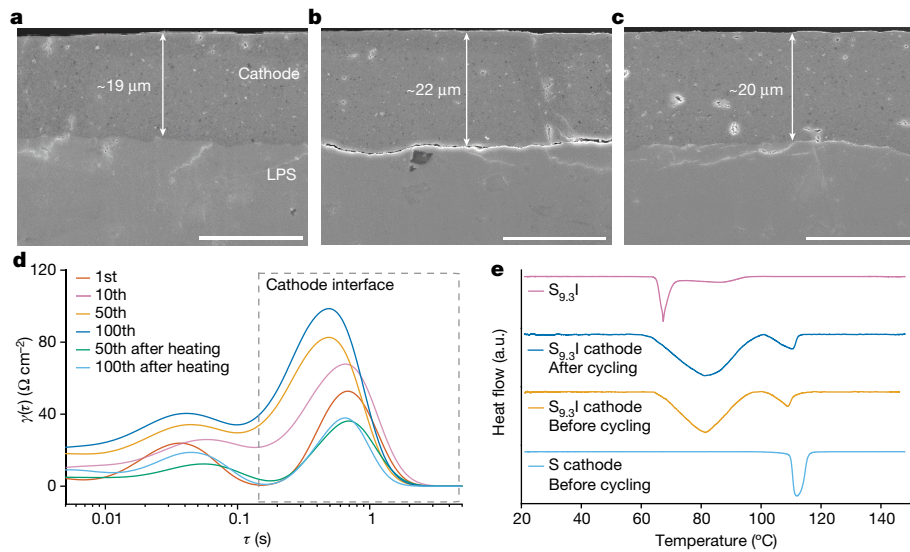


**Fig. 4 | Repair of the  $S_{9.3}I$  cathode/LPS solid electrolyte interface in  $Li-S_{9.3}I$  cells by remelting.** **a–c**, Cross-sectional SEM images of  $S_{9.3}I$  cathode/LPS interface at 25 °C: before cycling (a), after 50 cycles (b) and after reheating at 100 °C after 50 cycles (c). **d**, DRT analysis of EIS data of the  $Li-S_{9.3}I$  full cell after

different cycles at 25 °C. **e**, DSC curves of S and  $S_{9.3}I$  cathodes before and after the initial cycle along with that of pristine  $S_{9.3}I$ . Scale bars, 20  $\mu\text{m}$ .  $\tau$ , relaxation time;  $\gamma(\tau)$ , distribution function of relaxation times.

$\text{LiS}_x$  in  $\text{S}_{9.3}\text{I}$  cathodes discharged to 1.3 V and the chemically lithiated  $\text{S}_{9.3}\text{I}$  is further confirmed by ultraviolet-visible (UV-Vis) spectroscopy analysis of their tetrahydrofuran (THF) solution (Extended Data Fig. 9h,i). Overall, the formation of  $\text{LiS}_x$  during cycling is an essential feature of the working mechanism of  $\text{S}_{9.3}\text{I}$  cathode. Further XRD analysis confirms the presence of  $\text{Li}_2\text{S}$  in chemically lithiated  $\text{S}_{9.3}\text{I}$  (Extended Data Fig. 10a). Cryo-transmission electron microscopy (cryo-TEM), EDX and Li electron energy loss spectroscopy (EELS) indicate a homogeneous distribution of S, I and Li species over the bulk area of the sample (Fig. 3c, Extended Data Fig. 10b,c and Methods), implying no phase segregation. The S:I atomic ratio in lithiated  $\text{S}_{9.3}\text{I}$  determined by EDX is 9.6:1, very close to the theoretical ratio.

The evolution of the cathode/electrolyte interface during cycling is investigated by cross-sectional SEM. In the as-prepared cell (Fig. 4a), the  $\text{S}_{9.3}\text{I}$  cathode is around 19  $\mu\text{m}$  thick and shows intimate interfacial contact with the LPS layer. After 50 cycles at 25 °C, interfacial voids are observed (Fig. 4b), presumably owing to the volume change of the cathode during cycling. The thickness of the cathode layer also increases to about 22  $\mu\text{m}$ , pointing to further porosity buildup inside the cathode composite. The electrode undergoes melt-driven in situ interfacial repair after being heated to 100 °C followed by cooling back to 25 °C (Fig. 4c). The S:I ratio inside the cathode after repeated heating–cooling processes shows negligible change (Extended Data Fig. 10d,e). Interfacial repair by heating also manifests itself in EIS (Extended data Fig. 10f,g) and distribution of relaxation times (DRT) analyses (Fig. 4d). Relaxation times in the range of 0.1–1 s are associated with the impedance of ion transport across the cathode interface<sup>33,34</sup>. The interfacial impedance continuously increases from the first cycle to the 50th cycle, but is reduced by reheating to the value after the first cycle. A similar restoration is observed at the 100th cycle as well. Reheating is thus highly effective in healing the cathode interface as demonstrated in the cycling stability shown in Fig. 2c. Melt-driven in situ repair of the interface is enabled by the low melting point of  $\text{S}_{9.3}\text{I}$ , which is supported by DSC data (Fig. 4e).

Overall, the design of this conducting sulfur iodide molecular crystal material with a low melting point expands the scope of solid-state chemistry of sulfur. Iodine contributes new states inside the band gap of sulfur to introduce electronic conductivity and promotes the formation of  $\text{LiS}_x$  species, which are essential in increasing the reactivity of sulfur cathode. The discovery of the sulfur iodide material might inspire searches for other sulfur materials that have even lower melting points and higher conductivities.

## Online content

Any methods, additional references, Nature Portfolio reporting summaries, source data, extended data, supplementary information, acknowledgements, peer review information; details of author contributions and competing interests; and statements of data and code availability are available at <https://doi.org/10.1038/s41586-024-07101-z>.

- Bruce, P. G., Freunberger, S. A., Hardwick, L. J. & Tarascon, J. M. Li-O<sub>2</sub> and Li-S batteries with high energy storage. *Nat. Mater.* **11**, 19–29 (2011).
- Randau, S. et al. Benchmarking the performance of all-solid-state lithium batteries. *Nat. Energy* **5**, 259–270 (2020).
- Yang, Z., Huang, H. & Lin, F. Sustainable electric vehicle batteries for a sustainable world: perspectives on battery cathodes, environment, supply chain, manufacturing, life cycle, and policy. *Adv. Energy Mater.* **12**, 2200383 (2022).
- Yue, J., Yan, M., Yin, Y. X. & Guo, Y. G. Progress of the interface design in all-solid-state Li-S batteries. *Adv. Funct. Mater.* **28**, 1707533 (2018).

- Guo, W. et al. Artificial dual solid-electrolyte interfaces based on in situ organothiol transformation in lithium sulfur battery. *Nat. Commun.* **12**, 3031 (2021).
- Fu, K. et al. Three-dimensional bilayer garnet solid electrolyte based high energy density lithium metal-sulfur batteries. *Energy Environ. Sci.* **10**, 1568–1575 (2017).
- Lin, Z., Liu, Z. C., Dudney, N. J. & Liang, C. D. Lithium superionic sulfide cathode for all-solid lithium-sulfur batteries. *ACS Nano* **7**, 2829–2833 (2013).
- Ji, X., Lee, K. T. & Nazar, L. F. A highly ordered nanostructured carbon-sulphur cathode for lithium-sulphur batteries. *Nat. Mater.* **8**, 500–506 (2009).
- Pan, H. et al. Carbon-free and binder-free Li-Al alloy anode enabling an all-solid-state Li-S battery with high energy and stability. *Sci. Adv.* **8**, eabn4372 (2022).
- Yang, X., Luo, J. & Sun, X. Towards high-performance solid-state Li-S batteries: from fundamental understanding to engineering design. *Chem. Soc. Rev.* **49**, 2140–2195 (2020).
- Wu, J., Liu, S., Han, F., Yao, X. & Wang, C. Lithium/sulfide all-solid-state batteries using sulfide electrolytes. *Adv. Mater.* **33**, 2000751 (2021).
- Nagao, M., Hayashi, A. & Tatsumisago, M. High-capacity  $\text{Li}_2\text{S}$ -nanocarbon composite electrode for all-solid-state rechargeable lithium batteries. *J. Mater. Chem.* **22**, 10015–10020 (2012).
- Chen, Z. et al. Bulk/interfacial synergistic approaches enable the stable anode for high energy density all solid-state lithium-sulfur batteries. *ACS Energy Lett.* **7**, 2761–2770 (2022).
- Yao, X. et al. High performance all-solid-state lithium-sulfur batteries enabled by amorphous sulfur-coated reduced graphene oxide cathodes. *Adv. Energy Mater.* **7**, 1602923 (2017).
- Saßnick, H. D. & Cocchi, C. Electronic structure of cesium-based photocathode materials from density functional theory: performance of PBE, SCAN, and HSE06 functionals. *Electron. Struct.* **3**, 027001 (2021).
- Hautier, G. et al. Phosphates as lithium-ion battery cathodes: an evaluation based on high-throughput ab initio calculations. *Chem. Mater.* **23**, 3495–3508 (2011).
- Liu, G., Niu, P., Yin, L. & Cheng, H.-M.  $\alpha$ -Sulfur crystals as a visible-light-active photocatalyst. *J. Am. Chem. Soc.* **134**, 9070–9073 (2012).
- Abass, A. K. & Ahmad, N. H. Indirect band gap investigation of orthorhombic single crystals of sulfur. *J. Phys. Chem. Solids* **47**, 143–145 (1986).
- Chen, X. et al. Dynamically preferred state with strong electronic fluctuations from electrochemical synthesis of sodium manganite. *Matter* **5**, 735–750 (2022).
- Lee, Y. G. et al. High-energy long-cycling all-solid-state lithium metal batteries enabled by silver-carbon composite anodes. *Nat. Energy* **5**, 299–308 (2020).
- Ye, L. & Li, X. A dynamic stability design strategy for lithium metal solid state batteries. *Nature* **593**, 218–222 (2021).
- Li, C. et al. A quasi-intercalation reaction for fast sulfur redox kinetics in solid-state lithium-sulfur batteries. *Energy Environ. Sci.* **15**, 4289–4300 (2022).
- Zhang, H. et al. Designer anion enabling solid-state lithium-sulfur batteries. *Joule* **3**, 1689–1702 (2019).
- Zhang, Y. et al. Se as eutectic accelerator in sulfurized polyacrylonitrile for high performance all-solid-state lithium-sulfur battery. *Energy Storage Mater.* **21**, 287–296 (2019).
- Li, X. et al. High-performance Li-SeS all-solid-state lithium batteries. *Adv. Mater.* **31**, 1808100 (2019).
- Li, M. et al. Solid-state lithium-sulfur battery enabled by thio-LiICON/polymer composite electrolyte and sulfurized polyacrylonitrile cathode. *Adv. Funct. Mater.* **30**, 1910123 (2020).
- Wang, D. et al. Realizing high-capacity all-solid-state lithium-sulfur batteries using a low-density inorganic solid-state electrolyte. *Nat. Commun.* **14**, 1895 (2023).
- Liu, Y., Meng, X., Wang, Z. & Qiu, J. A Li-S-based all-solid-state battery with high energy and superior safety. *Sci. Adv.* **8**, eabl8390 (2022).
- Patel, M. U. et al. X-ray absorption near-edge structure and nuclear magnetic resonance study of the lithium-sulfur battery and its components. *ChemPhysChem* **15**, 894–904 (2014).
- Liang, X. et al. A highly efficient polysulfide mediator for lithium-sulfur batteries. *Nat. Commun.* **6**, 5682 (2015).
- Nandasiri, M. I. et al. In-situ chemical imaging of solid-electrolyte interphase layer evolution in Li-S batteries. *Chem. Mater.* **29**, 4728–4737 (2017).
- Yang, C. et al. Unique aqueous Li-ion/sulfur chemistry with high energy density and reversibility. *Proc. Natl. Acad. Sci. USA* **114**, 6197–6202 (2017).
- Li, X. et al. Highly stable halide-electrolyte-based all-solid-state Li-Se batteries. *Adv. Mater.* **34**, 2200856 (2022).
- Lu, Y., Zhao, C. Z., Huang, J. Q. & Zhang, Q. The timescale identification decoupling complicated kinetic processes in lithium batteries. *Joule* **6**, 1172–1198 (2022).

**Publisher's note** Springer Nature remains neutral with regard to jurisdictional claims in published maps and institutional affiliations.

Springer Nature or its licensor (e.g. a society or other partner) holds exclusive rights to this article under a publishing agreement with the author(s) or other rightsholder(s); author self-archiving of the accepted manuscript version of this article is solely governed by the terms of such publishing agreement and applicable law.

© The Author(s), under exclusive licence to Springer Nature Limited 2024

## Methods

### Materials

The following materials were used: sulfur powder (Sigma-Aldrich, >99.98%), iodine powder (Sigma-Aldrich, >99.99%), vapour grown carbon fibre (VGCF; Sigma-Aldrich, >99.99%, length: approximately 2–10 µm, diameter: about 200 nm), LPS (NEI, ion conductivity (25 °C): approximately  $1 \times 10^{-4}$  S cm<sup>-1</sup>, size: about 3–5 µm), Li<sub>6</sub>PS<sub>5</sub>Cl (LPSCl; NEI, ion conductivity (25 °C):  $9.3 \times 10^{-4}$  S cm<sup>-1</sup>, size: about 3–5 µm), SP (MTI, about 40 nm), Li foils (China Energy Lithium, >99.95%, about 250 µm and about 50 µm), Li powder (China Energy Lithium, >97%, 25–60 µm), THF (anhydrous, Sigma-Aldrich, >99.99%) and Li<sub>2</sub>S powder (Sigma-Aldrich, >99.98%).

### Preparation of sulfur iodide materials

Sulfur iodide materials with different sulfur to iodine ratios were prepared by a two-step procedure. Typically, 1.0 g of S/I mixtures with different ratios were first prepared by grinding stoichiometric amounts of sulfur powder and iodine powder using a mortar and pestle in the air for 10 min. The sulfur iodide materials were then obtained by melting the preprepared S/I mixtures in a small vial (20 ml) at 80 °C for 3 h with a heating rate of 1 °C min<sup>-1</sup> followed by a natural cooling procedure. The density of liquid S<sub>9.3</sub>I at 80 °C and 100 °C was measured to be approximately 2.35 and approximately 2.32 g cm<sup>-3</sup>, respectively. The bulk modulus of S<sub>9.3</sub>I measured by compression test was 0.29 GPa at 25 °C, which is much smaller than 7.7 GPa of α-S (ref. 35). The viscosity of liquid S<sub>9.3</sub>I increases from approximately 81 to approximately 196 mPa·s when the temperature increases from 80 °C to 100 °C. This behaviour is associated with the increase of the mass fraction of polymeric S chains which can cause more entanglement<sup>36</sup>.

### Preparation of S<sub>9.3</sub>I–LPS–VGCF cathode composite

The as-synthesized sulfur iodide pellets were crushed into powders using mortar and pestle. A mixture composed of S<sub>9.3</sub>I powder, LPS and VGCF with a weight ratio of 4:4:2 was loaded into a 100 ml ball-milling jar inside a glovebox (O<sub>2</sub> and moisture below 0.5 ppm) and milled at 500 rpm for 10 h. The weight ratio of ball-milling beads to the cathode composite was around 40:1. The S–LPS–VGCF cathode composite was prepared with the same procedure as the S<sub>9.3</sub>I–LPS–VGCF cathode.

### Cell fabrication

**Li/SP/LPSCl/SP/Li symmetric cells.** First, 200 mg of LPSCl powder was loaded into a poly(ether-ether-ketone) (PEEK) die with a diameter of 13 mm and two titanium electrodes block on both sides. A pressure of approximately 30 MPa was applied to press the loose LPSCl powder into the die. After that, about 4–5 mg cm<sup>-2</sup> of SP powder was loaded on both sides of the LPSCl pellet and a high pressure of 360 MPa was applied for densification. Finally, two pieces of Li foils (around 250 µm) were assembled into the symmetric cells with a pressure of approximately 30 MPa.

**Li/SP/LPSCl/LPS/cathode full cells.** First, 180 mg of LPS powder was loaded into a PEEK die with two titanium electrodes and pressed with a pressure of 30 MPa. Subsequently, 60 mg of LPSCl powder was pressed on one side of the prepressed LPS pellet at 30 MPa. Then, 4–5 mg cm<sup>-2</sup> of SP powder and about 3 mg cm<sup>-2</sup> of cathode powder were pressed on the LPSCl and LPS sides, respectively, at 30 MPa. A high pressure of 360 MPa was then used to press the SP/LPSCl/LPS/cathode composite together for 5–10 min. A piece of Li foil (around 50 µm) was then attached to the SP surface to complete the assembly of the solid-state full cells. A pressure of 30 MPa was maintained during cycling tests and periodical interface repair by heating. The full cells with high mass loading cathodes were assembled using the same procedure except with a mass loading of 10.5 mg cm<sup>-2</sup> of the cathode composite. It should be noted that the viscosity of liquid S<sub>9.3</sub>I at 80 °C and 100 °C is approximately

81 and approximately 196 mPa·s, respectively, which greatly limits its flowability in a composite cathode. To further prevent any leakage at elevated temperatures during cycling, we designed a Swagelok cell in which the size difference between the titanium piston and the PEEK die cylinder was ≤0.1 mm. To prevent the liquid cathode from flowing into the LPS solid state electrolyte layer, we placed the cathode at the bottom and the anode on top for battery tests when running above the melting point of the cathode. Moreover, LPS becomes much denser than LPSCl after heating at 100 °C. As a result, the Li–S<sub>9.3</sub>I full cells were heat treated at this temperature before further testing. A dense LPS layer can help prevent any diffusion of the liquefied S<sub>9.3</sub>I cathode, although its high viscosity makes such diffusion unlikely.

### Electrochemical characterization

Before the electrochemical performance tests, all of the symmetric cells and full cells were heated at 100 °C for 3 h with a heating rate of 1 °C min<sup>-1</sup> followed by natural cooling procedures in the oven. After that, cells underwent galvanostatic cycling at different temperatures on a LAND battery test system after resting for 3 h. To measure the long-term cycling stability of the SP interlayer for protecting the lithium metal anode, an Li/Li symmetric cell was cycled at constant current density of 0.3 mA cm<sup>-2</sup> and a capacity of 0.3 mAh cm<sup>-2</sup>. The EIS tests were performed on a BioLogic VMP300t electrochemical workstation within a frequency range from 7 MHz to 0.01 Hz, and the corresponding DRT analysis was performed using techniques as previously reported<sup>37</sup>.

### XRD

Small-angle and wide-angle X-ray diffraction of different sulfur iodide materials were performed on a Rigaku Smartlab diffractometer with a Cu anode (K-alpha emission (Kα), wavelength  $\lambda = 1.5418$  Å). The primary beam power was set to be 1.76 kW. The sample stage was aligned normal to the sample surface. In situ XRD analysis (30–150 °C) of S<sub>9.3</sub>I powder during heating was performed on a Bruker D8 Discover diffractometer, which was equipped with a rotating Cu anode (Kα  $\lambda = 1.5418$  Å) and a Vantec 500 area detector. The XRD patterns were collected every 5 °C. Samples are sealed in a borosilicate capillary (0.8 mm diameter, approximately 0.01 mm thin-wall, Charles Supper) by using epoxy in an Ar-filled glovebox before being taken out for tests. The sample capillary with the Ti sample holder slit and an internal cartridge heater was placed on a custom-built programmable XYZ stage. For XRD measurements, 50 kV and 24 mA were applied. The XRD data were first processed with the Bruker-AXS GADDS software and further analysed by MDI JADE XRD software.

### Electrical conductivity tests

To measure the electrical conductivity of sulfur iodide materials with different ratios, 180 mg of sample was pressed in a peek die (diameter: 13 mm) with two titanium electrodes at 360 MPa. A constant voltage of 0.2 V, 0.4 V or 0.6 V was applied for 1 h, respectively, to measure the stabilized current on a BioLogic VMP300t electrochemical workstation. The thickness of the sample was confirmed by SEM. On the basis of the voltage, current and the thickness of samples, the electrical conductivity can be calculated.

### SEM

SEM (FEI Quanta 250 SEM) with EDX was used to determine the morphology and chemical composition of the S<sub>9.3</sub>I sample under 30 kV and 0.1 nA. The cross-sectional images of S<sub>9.3</sub>I/LPS and S/LPS mixtures were collected using cryo-focused ion beam-scanning electron microscopy (FEI Scios, Scios DualBeam) at 5 kV and 0.1 nA. The cross-sections were first cut with an ion beam of 30 nA, followed by a surface cleaning process at 0.1 nA. For the cross-sectional SEM analysis of cathode and anode interfaces in the full cells, the samples were prepared by an Argon-ion beam cross-section polisher (IB-19520CCP) developed by JEOL. An accelerating voltage of 4 kV and a milling rate of around 25 µm h<sup>-1</sup> were

used to minimize artifacts. During milling, the sample stage was placed perpendicular to the ion beam and swung automatically within  $\pm 30^\circ$  to broaden the polished area and avoid beam strains. An air-free vessel was used to transfer samples between the glovebox and characterization tools. The cross-sectional SEM images of cathode and anode interfaces were conducted in Axia ChemiSEM.

### Cryo-TEM

To prepare samples for the tests, a sample suspension in hexane was drop cast on a gold transmission electron microscopy (TEM) grid in a glovebox to prevent air and water exposure. The TEM grid was then loaded on a Gatan cryo-holder in a liquid N<sub>2</sub> environment. The holder tip shutter was closed after loading the TEM grid on the holder and during the transfer to the microscope. The sample was kept at liquid N<sub>2</sub> temperature in the TEM (FEI Talos F200x microscope) to reduce radiation damage, and characterized using scanning electron microscopy transmission, EDX (FEI Super-X EDX system) and EELS (Gatan Enfinium). The presence of Li in the sample was confirmed by EELS, which showed a peak at approximately 60 eV, an indication of energy loss at the Li K-edge. The presence of S and I elements in the sample was confirmed by EDX. The composite map of S, I was acquired using EDX spectra, and the map of Li was done by EELS spectra. It should be noted that the chemically lithiated S<sub>9,3</sub>I sample was still very sensitive to the electron beam even in the cryo-TEM. To reduce the beam damage, a low electron dose was applied for EDX and EELS during tests. In addition, a suitable particle size should be selected to balance the needs of reducing the radiation damage and of a thinner sample for EELS signal acquisition.

### X-band EPR

X-band EPR measurements were conducted on a Bruker EMXplus EPR spectrometer. All samples were packed into Q-band tubes inside an Ar-filled glovebox and sealed with epoxy. The Q-band tubes were inserted into 4 mm quartz EPR tubes to hold the samples in place inside the resonator cavity. Variable temperature measurements were performed using an X-band Dual Mode EPR resonator (Bruker ER 4119DM). The sample was allowed to equilibrate at the desired temperatures for 10 min before each measurement. Ex situ measurements performed on the S<sub>9,3</sub>I cathode samples at room temperature used a high sensitivity EPR resonator (Bruker ER 4119HS-LC). All measurements were carried out with 2 mW of power, a 100 kHz modulation frequency and a modulation amplitude of 4 Gauss. Spectral fits were conducted with EasySpin<sup>38</sup>.

### XPS

The cathode layers were separated from the solid state electrolyte layer by cracking the pellet cells and the conductive tapes were used to fix cathode samples on the XPS sample holders. The XPS tests were conducted on a Kratos Ultra DLD to study the chemical composition and valence states of the elements in the samples with a spot size ranging 300  $\mu\text{m}$  to 700  $\mu\text{m}$ . All of the samples were transported into XPS equipment through a connected Ar-filled glovebox to avoid any air exposure. XPS spectra were acquired with a 0.1 eV resolution for C1s, S2p and I3d regions. The analysis of XPS spectra was performed using CasaXPS software.

### XAS

The iodine L<sub>2</sub>-edge absorption spectra were measured at fluorescence mode at beamline 7-BM of the National Synchrotron Light Source II (NSLS II) at Brookhaven National Laboratory (BNL). Each spectrum takes 15 seconds, and 50 spectra were merged to get the final data for improving the signal-to-noise ratio. The sulfur K-edge spectra were collected in fluorescence mode at the 8-BM beamline of the National Synchrotron Light Source II (NSLS II) at Brookhaven National Laboratory (BNL). All the XAS results were analysed using the Athena software package<sup>39</sup>.

### PDF

For PDF measurements, the sample powders were packed inside polyimide capillary (Cole-Parmer) tubes sealed by epoxy glue at the end. The PDF data were collected at the 28-ID-2 beamline of the NSLS II at BNL using a photon wavelength of 0.18475 Å. The obtained data were integrated using Fit2D software<sup>40</sup>. The PDF and atomic pair distribution function ( $G(r)$ ) values were extracted using PDFgetX3 software<sup>41</sup>. For the in situ heating PDF experiment, the sample was heated from room temperature (293 K) to 403 K, and cooled back to 293 K with a step size of 5 K.

### UV-Vis spectroscopy

Typically, 20 mg of powder samples was added into 4 ml of THF and then the THF solutions were obtained by centrifugation over several minutes. To prepare the standard Li<sub>2</sub>S<sub>4</sub> and Li<sub>2</sub>S<sub>6</sub> THF solutions, stoichiometric amounts of Li<sub>2</sub>S and S powder were added into 10 ml of THF with a targeted concentration of 0.2 mmol l<sup>-1</sup>. Afterwards, the solution and powder mixtures were vigorously stirred over 5 days until fully dissolved. The measurements of samples were performed on a Hitachi UH4150 UV-Vis spectrophotometer.

### DSC

10 mg of a powder sample was sealed in a 40  $\mu\text{l}$  Al pan with a lid inside an Ar-filled glovebox. The samples were measured on a TA Instruments Discovery Series DSC 2500 within the temperature window of 20–150 °C at a heating rate of 5 °C min<sup>-1</sup>.

### Raman spectroscopy

Raman measurements were performed on a Perkin Elmer RamanStation 400F with a laser wavelength of 785 nm. The air sensitive samples were sealed between two quartz wafers with Kapton film covering the edges.

### Mass spectrometry

Laser desorption ionization-time-of-flight mass spectrometry (LDI-TOFMS) analysis was performed at the Molecular MS Facility at UC San Diego, using a Bruker AutoFlex Max matrix-assisted laser desorption ionization-time-of-flight mass spectrometry (MALDI-TOFMS) instrument. The LDI-TOFMS measurement was operated under negative ion mode. Laser energy was optimized and set at 10% for 'soft' ionization and minimal fragmentation. LDI-TOFMS data were acquired using Bruker flexControl software (v.3.4) and analysed using Bruker flexAnalysis software (v.3.4).

### Computational details

**DFT parameters.** The DFT calculations were carried out using the projector augmented wave (PAW) approach<sup>42</sup> as implemented in the Vienna Ab initio Simulation Package (VASP)<sup>43</sup>. Structure relaxation was performed with the SCAN meta-GGA functional. The calculations of the electronic structure (DOS) were performed using the HSE functional<sup>44</sup> as well as the SCAN functional. All the calculations were spin polarized with an energy cutoff of 520 eV. The energy and force convergence criteria were set to 10<sup>-4</sup> eV and 0.05 eV Å<sup>-1</sup>, respectively. For the S unit cell and its derived structures, a  $\Gamma$ -centred  $k$ -points mesh of  $2 \times 1 \times 1$  was used. For DOS calculations a finer  $k$ -points mesh of  $2 \times 2 \times 2$  was used. The DFT-optimized minimum energy structures were used to perform Bader charge analysis<sup>45</sup>. All the input generation and output analyses were performed using Python Materials Genomics (pymatgen)<sup>46</sup>.

**S<sub>x</sub>I candidate structure generation.** S<sub>x</sub>I candidates at different S:I ratios were obtained by replacing S<sub>8</sub> rings with I<sub>2</sub> or I<sub>3</sub> molecules in octasulfur S unit cells (16 S<sub>8</sub> rings). The I<sub>2</sub> or I<sub>3</sub> molecules were placed at the site of S<sub>8</sub> rings in two possible orientations: parallel to the  $a-b$  plane along the S<sub>8</sub> molecular plane or perpendicular to the S<sub>8</sub> molecular

# Article

plane. Structure enumeration was performed to obtain several distinct site orderings per composition. In addition, the effect of orientational disorder was considered by placing  $I_2$  or  $I_3$  molecules at different combinations of orientations. The dimensions of the supercell size were  $10.587\text{ \AA} \times 12.952\text{ \AA} \times 24.567\text{ \AA}$ , which is the same as the unit cell parameter.

## Data availability

The data that support the findings of this study are available from the corresponding author upon request.

35. Guo, Q., Lau, K. C. & Pandey, R. Thermodynamic and mechanical stability of crystalline phases of  $\text{Li}_2\text{S}_2$ . *J. Phys. Chem. C* **123**, 4674–4681 (2019).
36. Sofekun, G. O. et al. The rheology of liquid elemental sulfur across the  $\lambda$ -transition. *J. Rheol.* **62**, 469–476 (2018).
37. Wan, T., Saccoccia, H. M., Chen, C. & Ciucci, F. Influence of the discretization methods on the distribution of relaxation times deconvolution: implementing radial basis functions with DRT tools. *Electrochim. Acta* **184**, 483–499 (2015).
38. Stoll, S. & Schweiger, A. EasySpin, a comprehensive software package for spectral simulation and analysis in EPR. *J. Magn. Reson.* **178**, 42–55 (2006).
39. Ravel, B. & Newville, M. ATHENA, ARTEMIS, HEPHAESTUS: data analysis for X-ray absorption spectroscopy using IFEFFIT. *J. Synchrotron Radiat.* **12**, 537–541 (2005).
40. Hammersley, A. P., Svensson, S. O., Hanfland, M., Fitch, A. N. & Hausermann, D. Two-dimensional detector software: from real detector to idealised image or two-theta scan. *High Press. Res.* **14**, 235–248 (1996).
41. Qiu, X., Thompson, J. W. & Billinge, S. J. L. PDFgetX2: a GUI-driven program to obtain the pair distribution function from X-ray powder diffraction data. *J. Appl. Crystallogr.* **37**, 678–678 (2004).
42. Blochl, P. E. Projector augmented-wave method. *Phys. Rev. B* **50**, 17953–17979 (1994).
43. Kresse, J. F. G. Efficient iterative schemes for ab initio total-energy calculations using a plane-wave basis set. *Phys. Rev. B* **54**, 1169–1186 (1996).
44. Heyd, J., Scuseria, G. E. & Ernzerhof, M. Hybrid functionals based on a screened Coulomb potential. *J. Chem. Phys.* **118**, 8207–8215 (2003).
45. Tang, W., Sanville, E. & Henkelman, G. A grid-based Bader analysis algorithm without lattice bias. *J. Phys. Condens. Matter* **21**, 084204 (2009).
46. Ong, S. P. et al. Python Materials Genomics ( pymatgen ): a robust, open-source python library for materials analysis. *Comput. Mater. Sci.* **68**, 314–319 (2013).

**Acknowledgements** This work was supported by the Advanced Research Projects Agency-Energy, US Department of Energy (DOE), under contract no. DE-AR0000781. M.L.H.C. and S.P.O. acknowledge the support from the Materials Project, funded by the US DOE, Office of Science, Office of Basic Energy Sciences, Materials Sciences and Engineering Division, under contract no. DEAC02-05-CH11231 (Materials Project Program No. KC23MP). Computing

resources were provided by the National Energy Research Scientific Computing Center (NERSC) and the Advanced Cyberinfrastructure Coordination Ecosystem: Services & Support (ACCESS) under grant no. DMR-150014. S.T. and E.H. are supported by the Assistant Secretary for Energy Efficiency and Renewable Energy (EERE), Vehicle Technology Office of the US DOE through the Advanced Battery Materials Research (BMR) Program under contract no. DE-SC0012704. This research used 28-ID-2, 8-BM and 7-BM beamlines of the National Synchrotron Light Source II, US DOE Office of Science User Facilities, operated for the DOE Office of Science by Brookhaven National Laboratory under contract no. DE-SC0012704. C. Wu, Z.F. and Y.Y. are supported by the US DOE's Office of EERE under the Vehicle Technologies Program under contract no. DE-EE0008864. This work made use of the shared facilities of the UC Santa Barbara MRSEC (grant no. DMR-720256), a member of the Materials Research Facilities Network (<http://www.mrfn.org>). This research used the Electron Microscopy facility of the Center for Functional Nanomaterials (CFN), which is a US DOE Office of Science User Facility, at Brookhaven National Laboratory, under contract no. DE-SC0012704. Canhui Wang and Chao Wang were supported by the Advanced Research Projects Agency-Energy, US DOE, under contract no. DE-AR00001191. FIB and SEM characterizations were performed at the San Diego Nanotechnology Infrastructure (SDNI) of UCSD supported by the NSF (grant no. ECCS1542148). Raman facilities were supported by the NSF through UCSD MRSEC, grant no. DMR-201192. The authors acknowledge the use of facilities and instrumentation at the UC Irvine (UCI) Materials Research Institute (IMRI), which was supported in part by the NSF through the UCI MRSEC (grant no. DMR-2011967). XPS facilities were funded in part by the NSF Major Research Instrumentation. We thank the Molecular Mass Spectrometry Facility at UC San Diego for performing the MALDI-TOFMS measurement, which is supported by the NSF under grant no. CHE-1338173. Part of this work was performed in the Cordx Yufeng Li Collaboratory.

**Author contributions** J.Z. and P.L. conceptualized the idea and designed all of the experiments. S.P.O. and M.L.H.C. performed the theoretical calculations and drafted the results. S.T. and E.H. conducted the XAS and X-ray PDF tests. S.W. performed the Raman, DSC, cryo-SEM and XPS measurements. C. Wu, Z.F. and Y.Y. collected the cross-sectional SEM images of the full cells at different states, including anode interfaces and cathode interfaces. H.N. collected EPR data, H.N. and R.J.C. analysed and wrote up the results. Canhui Wang and Chao Wang performed the cryo-TEM. Y.X. and E.E.F. performed the XRD tests. Q.R.S.M. did the in situ heating XRD test. H.L., S.Y., G.H., J. Holoubek, J. Hong and C.S. helped with the synthesis of materials, cell fabrications, electrochemical performance tests, data analysis, discussion and revision. C.J.B. helped with the revised manuscript preparation and discussion. J.Z., P.L. and S.P.O. drafted the manuscript with input and revision from all authors. P.L. and S.P.O. supervised the research. J.Z. and M.L.H.C. contributed equally to this work.

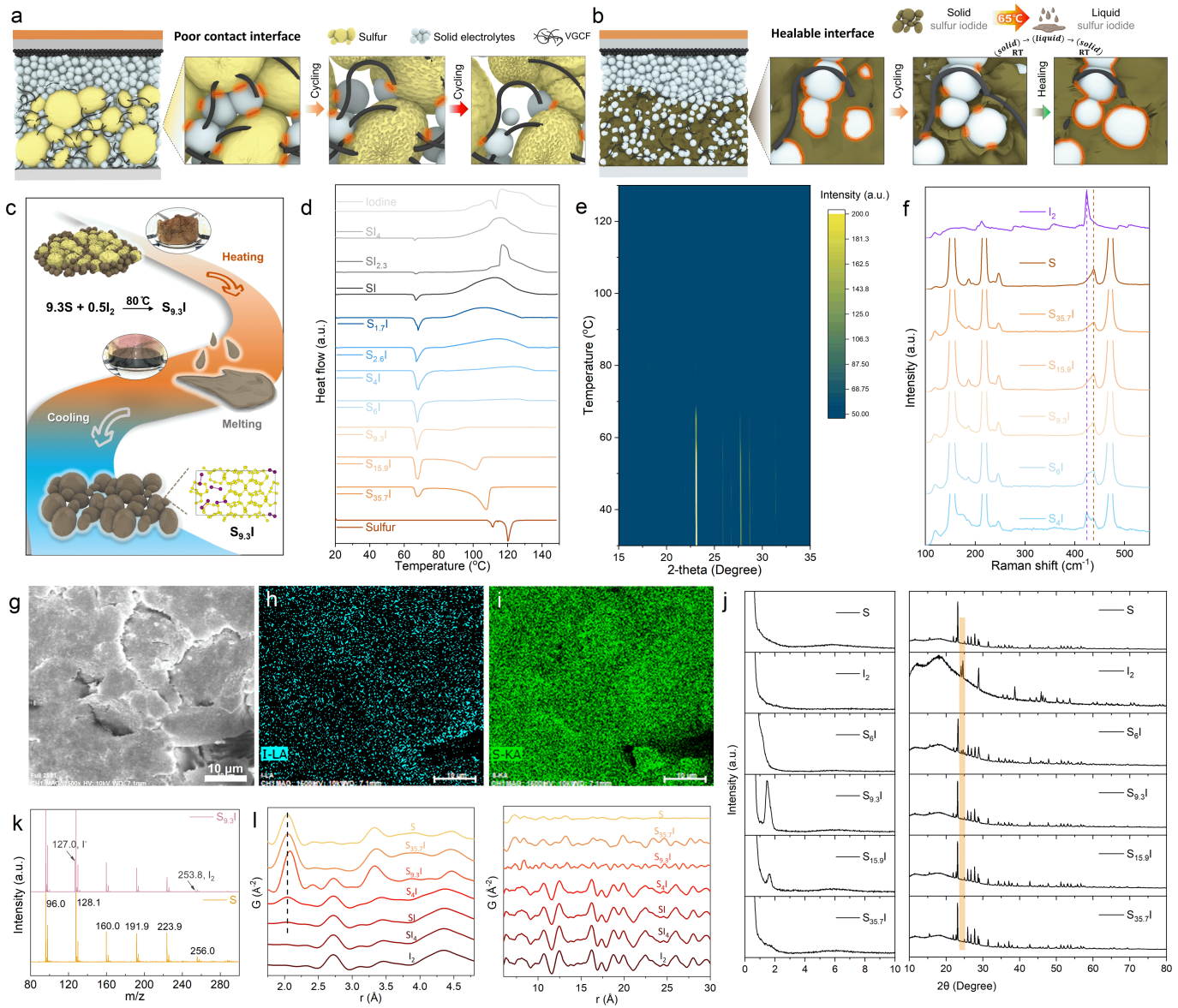
**Competing interests** P.L. and J.Z. report a US provisional patent application filed on February 13, 2023, Serial No. 63/484,659, based on this work.

## Additional information

**Correspondence and requests for materials** should be addressed to Shyue Ping Ong or Ping Liu.

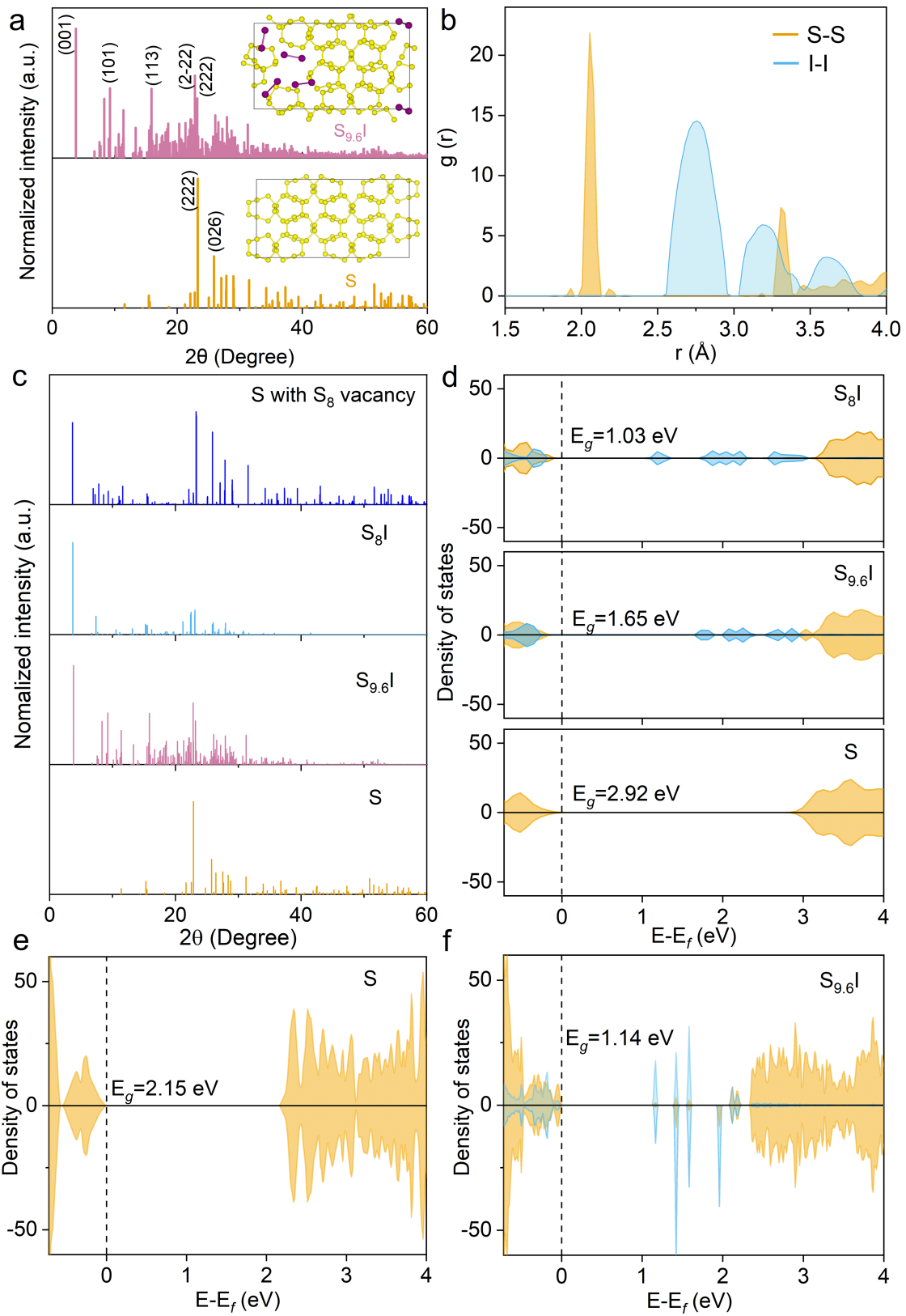
**Peer review information** *Nature* thanks Pouya Partovi-Azar and the other, anonymous, reviewer(s) for their contribution to the peer review of this work.

**Reprints and permissions information** is available at <http://www.nature.com/reprints>.



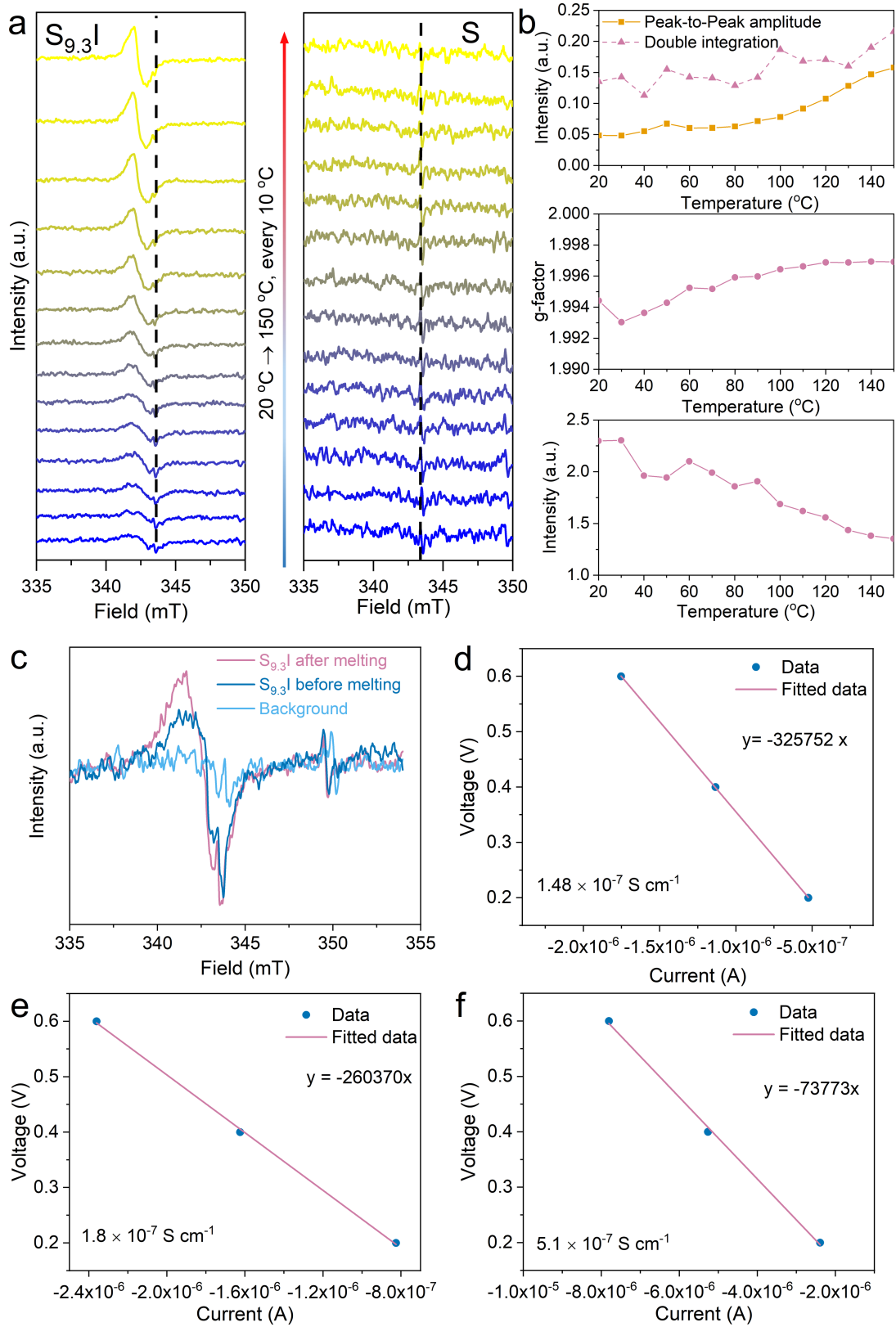
**Extended Data Fig. 1 | Healable interfaces in SSLSBs with a low-melting-point sulfur iodide, and the synthesis and characterization of sulfur iodide materials.** (a) Schematic of a solid state battery with elemental sulfur as the active material. Poor solid/solid contact develops during cycling due to volume changes of the active material. (b) Schematic of a solid state battery with sulfur iodide as the active material. Ideal active material/electrolyte interface is achieved through periodical heating to melt the cathode, thus healing the interface. (c) Illustration of the procedures to prepare  $S_{9.3}I$ . (d) The DSC curves of sulfur iodide with different S:I ratios in the temperature window of 20–150 °C. With S:I ratios decreasing from 1:0 to 9.3:1, the typical sulfur endothermic peak gradually disappears to transition to one phase melting behavior. Beyond 6:1, the exothermic peaks assigned to iodine are observed. (e) Spectra obtained during *in situ* heating XRD of  $S_{9.3}I$  from 30 to 130 °C with an 5 °C interval.

(f) Raman spectra of sulfur iodide with different ratios, which features an iodine peak located at  $423.8\text{ cm}^{-1}$  when the S:I ratio is less than 9.3:1. The cryo-SEM image (g) and the corresponding EDX mapping images of I (h) and S (i) element distribution of  $S_{9.3}I$  after melting. (j) XRD of S,  $I_2$ ,  $S_{35.7}I$ ,  $S_{15.9}I$ ,  $S_{9.3}I$ ,  $S_6I$ . In the low angle range, the relative intensity of the broadened peak centered at  $-1.5^\circ$  gradually increases with the increase of iodine, but from 9.3:1 to 6:1, the iodine diffraction peaks also emerge. (k) Mass spectra of S and  $S_{9.3}I$ . Compared to S,  $S_{9.3}I$  shows two additional peaks centered at 127.0 and 253.8 m/z, which are attributed to  $I^-$  and  $I_2$  species respectively. No peaks can be indexed to species containing S-I bonds. (l) The PDF of sulfur iodide materials after melting with different S:I ratios, elemental sulfur and iodine. When the ratio of S to I is below 9.3:1, bulk  $I_2$  is present as indicated by the signals from the short and long range structures.



**Extended Data Fig. 2 | Computed Crystal and electronic structure of S-I compounds.** (a) Computed XRD patterns of elemental S and predicted  $S_{9.6}$ I structure. (b) Computed PDF of  $S_{9.6}$ I. We attribute any minor discrepancies to the fact that the DFT relaxations are carried out at 0 K, while the experimental

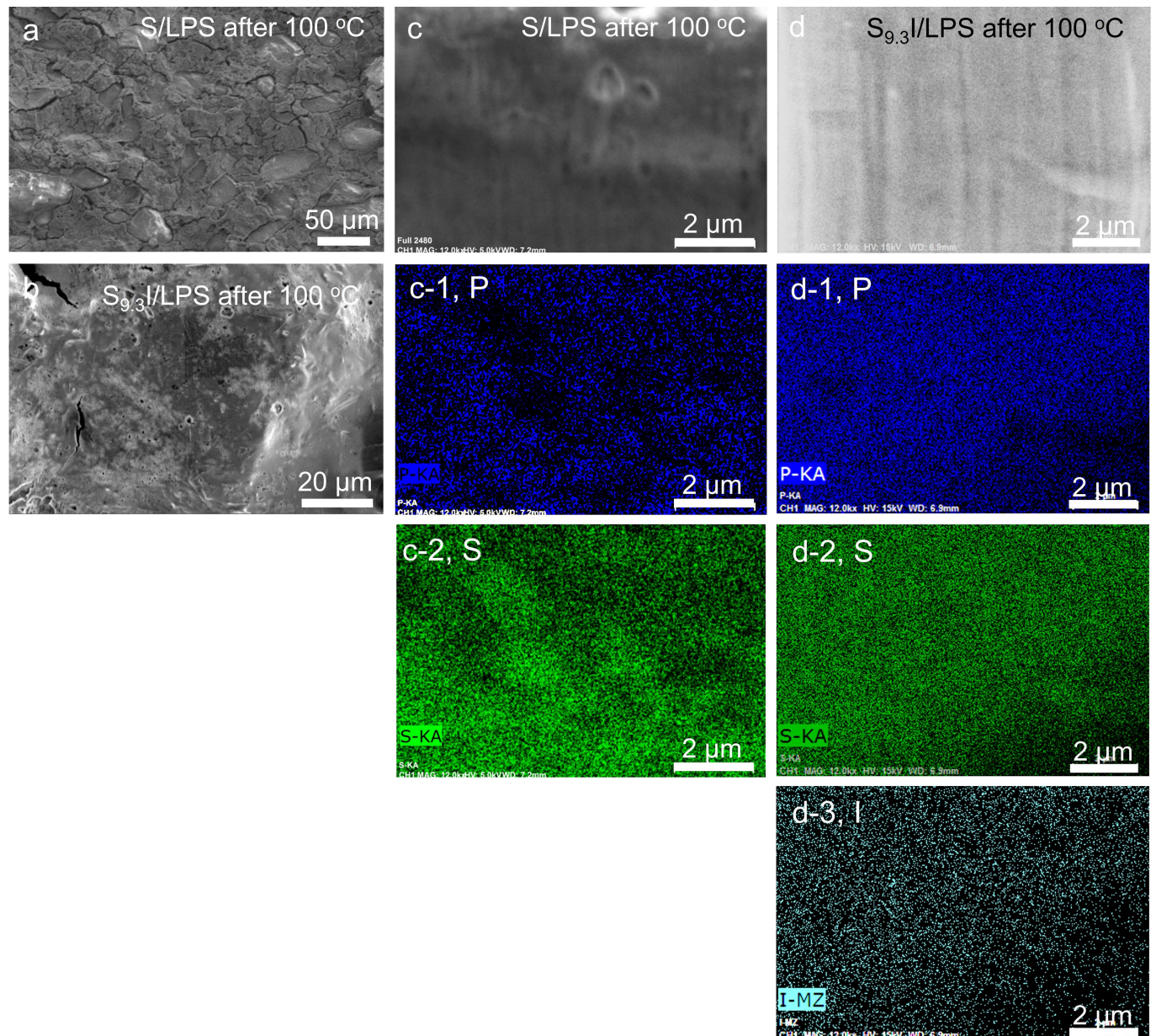
data is obtained at 300 K. (c) Computed XRD patterns of S,  $S_{9.6}$ I,  $S_8$ I and S with  $S_8$  ring vacancy structure. (d) HSE projected density of states of S,  $S_{9.6}$ I and  $S_8$ I. Elemental projected density of states for S (e) and  $S_{9.6}$ I (f) using SCAN functionals.



**Extended Data Fig. 3 | Electronic structure and conductivities of sulfur iodide materials.** (a) Variable temperature X-band EPR spectra collected on  $S_{9.3}I$  and elemental sulfur. The radical concentration in  $S_{9.3}I$  grows with increasing temperature, but not in  $S$ . (b) Temperature evolution of the EPR signal intensity (top panel), linewidth (bottom panel), and g-factor (middle panel) of  $S_{9.3}I$ . The g-factor for  $S_{9.3}I$  is approximately 1.99 and does not change appreciably with increasing temperature (bottom panel), suggesting that similar radical species are produced over the entire temperature range. (c) EPR spectra collected at 100 K on  $S_{9.3}I$  before and after melting. The electronic conductivity of  $S_{35.7}I$  (d),  $S_{15.9}I$  (e), and  $S_6I$  (f) measured by using a potentiostatic test at room temperature.

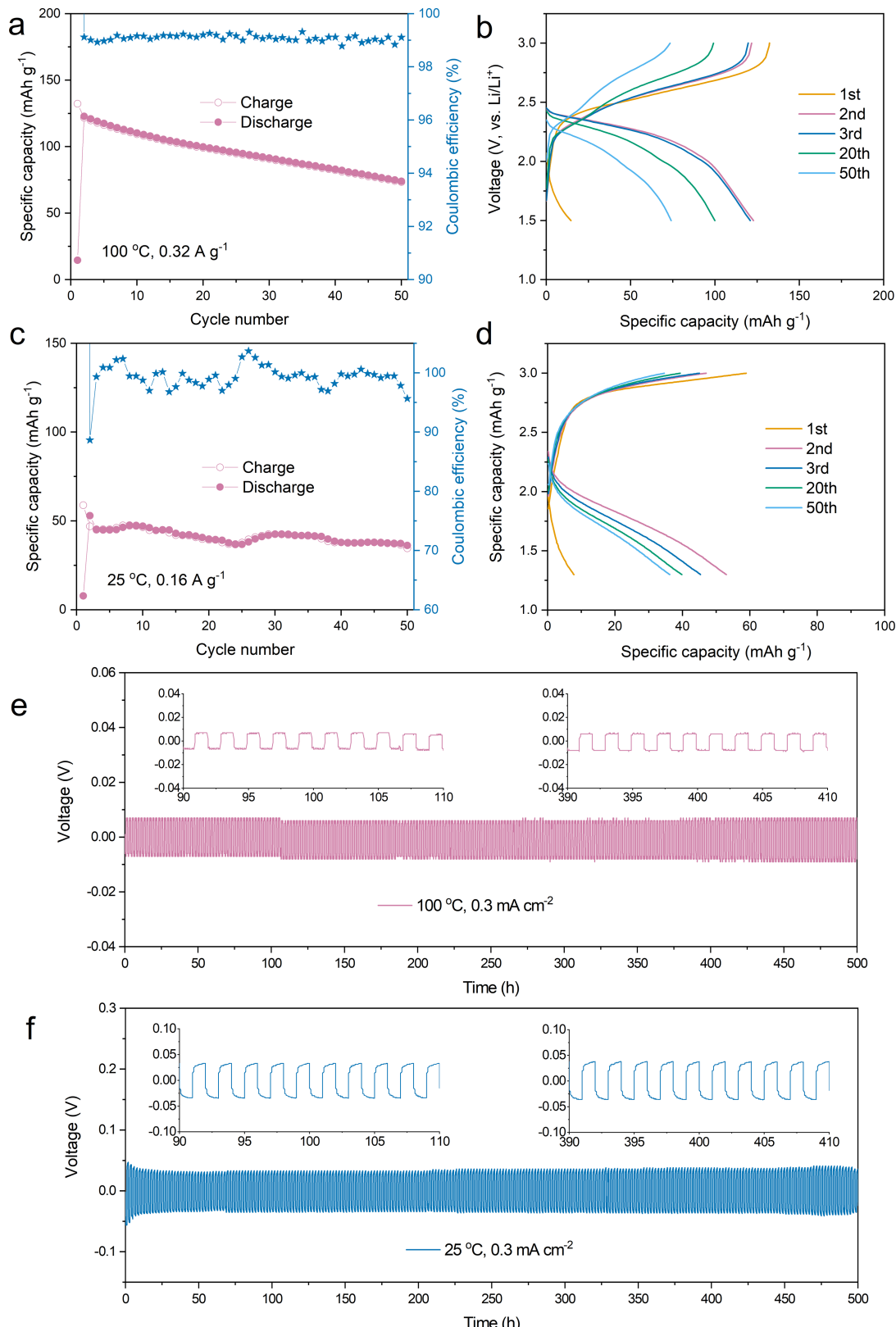
appreciably with increasing temperature (bottom panel), suggesting that similar radical species are produced over the entire temperature range. (c) EPR spectra collected at 100 K on  $S_{9.3}I$  before and after melting. The electronic conductivity of  $S_{35.7}I$  (d),  $S_{15.9}I$  (e), and  $S_6I$  (f) measured by using a potentiostatic test at room temperature.

# Article



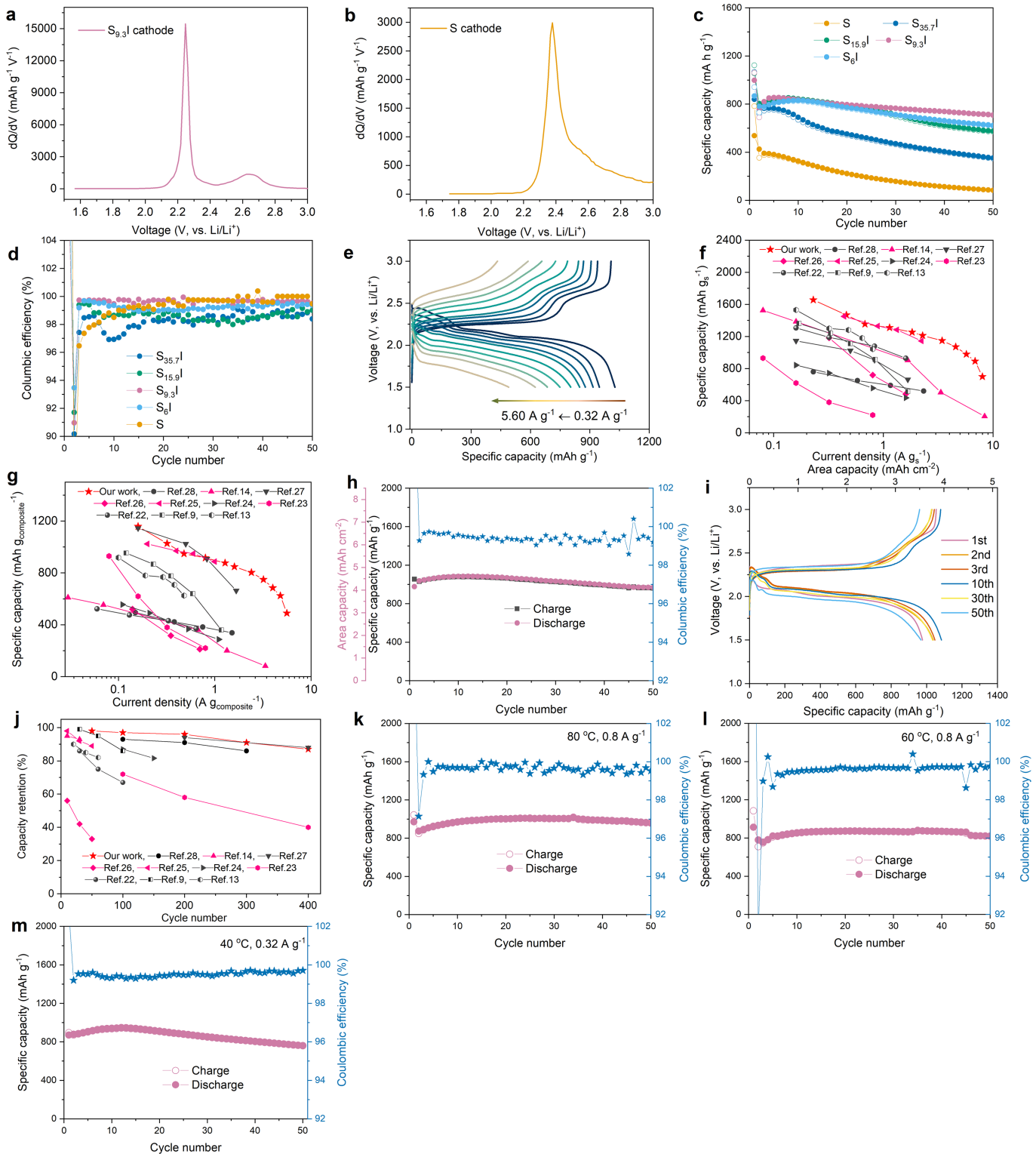
**Extended Data Fig. 4 | SEM and elemental mapping of S and S<sub>9.3</sub>I mixed with LPS after heating at 100 °C.** The SEM image of S/LPS mixture (a) and S<sub>9.3</sub>I/LPS mixture (b) after milling and heating at 100 °C. (c) The cross sectional cryo-FIB

SEM images and corresponding element distribution images of S/LPS for S and P. The distribution of S and P is inhomogeneous. (d) Distribution of S, P, and I in S<sub>9.3</sub>I/LPS. The distribution in the entire area is homogeneous.



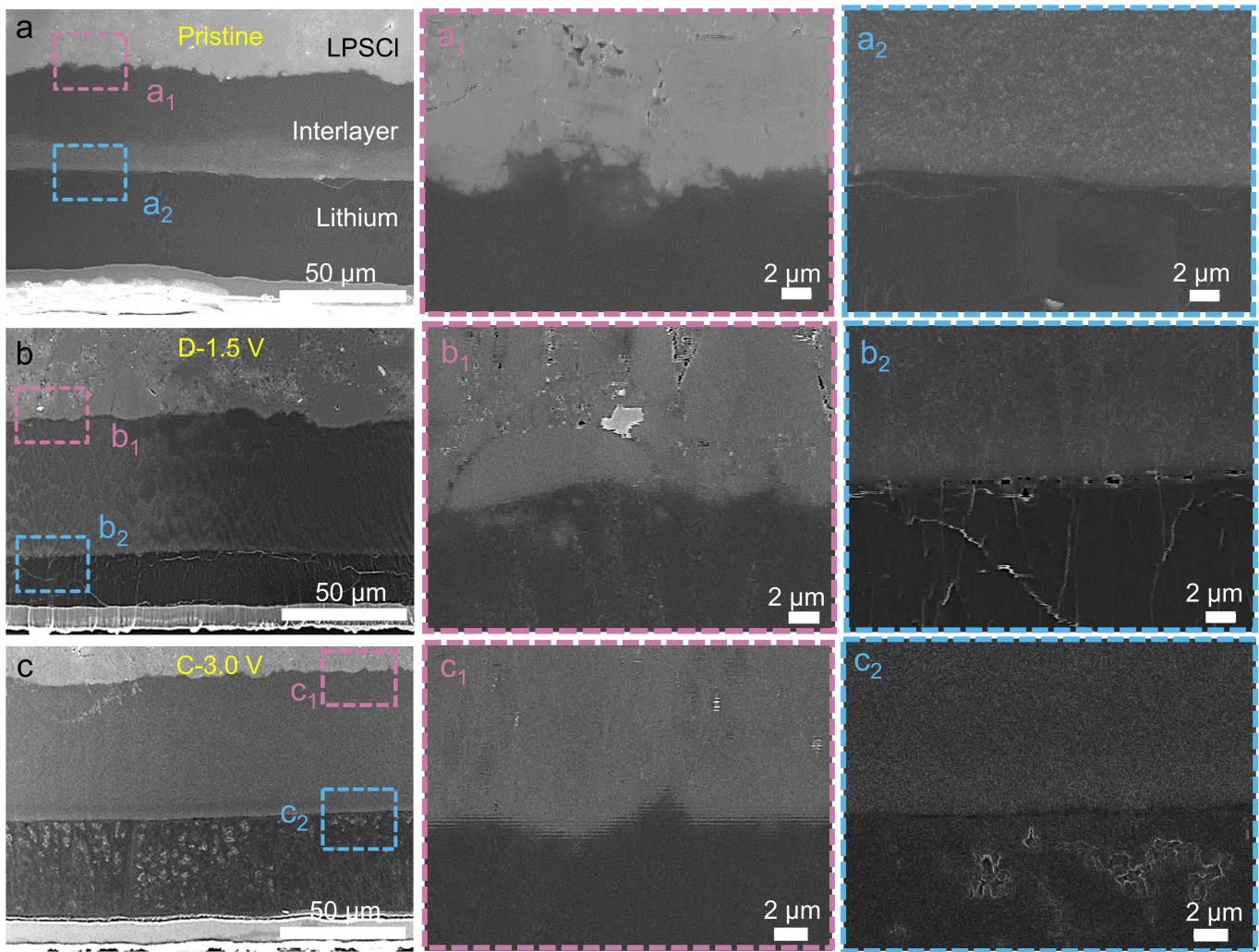
**Extended Data Fig. 5 | Electrochemical performance data of solid state cell components.** The cycling stability and capacity of a LPS/VGCF cathode at 100 °C (a) and 25 °C (c). The corresponding voltage profiles at 100 °C (b) and at 25 °C (d). Capacity contribution of LPS is very limited and the cycling stability

of LPS is very poor either at 100 °C or 25 °C with low coulombic efficiencies. The long-term cycling stability of Li/SP/LPSCI/SP/Li symmetric cells at 100 °C (e) and 25 °C (f) at a current density of 0.3  $\text{mA cm}^{-2}$ .



**Extended Data Fig. 6 | The performance of sulfur iodide cathode at different conditions and their comparison with other SSLSBs.** The dQ/dV curves during delithiation of S<sub>9.3</sub>I (a) and S (b) cathode based on the charging curves at 100 °C from Figs. 2a and b. (c) The cycling stability of S, S<sub>35.7</sub>I, S<sub>15.9</sub>I, S<sub>9.3</sub>I and S<sub>6</sub>I cathode at 1.6 A g<sup>-1</sup> and at 100 °C. (d) The corresponding cycling coulombic efficiency in (c). (e) Rate capability of S<sub>9.3</sub>I cathode at 100 °C at current densities of 0.32, 0.48, 0.80, 1.28, 1.60, 2.40, 3.20, 4.00, 4.80 and 5.60 A g<sup>-1</sup>. Rate performance comparison between Li-S<sub>9.3</sub>I solid state batteries with other reported SSLSBs: based on the weight of (f) only S and (g) S composite, red-colored

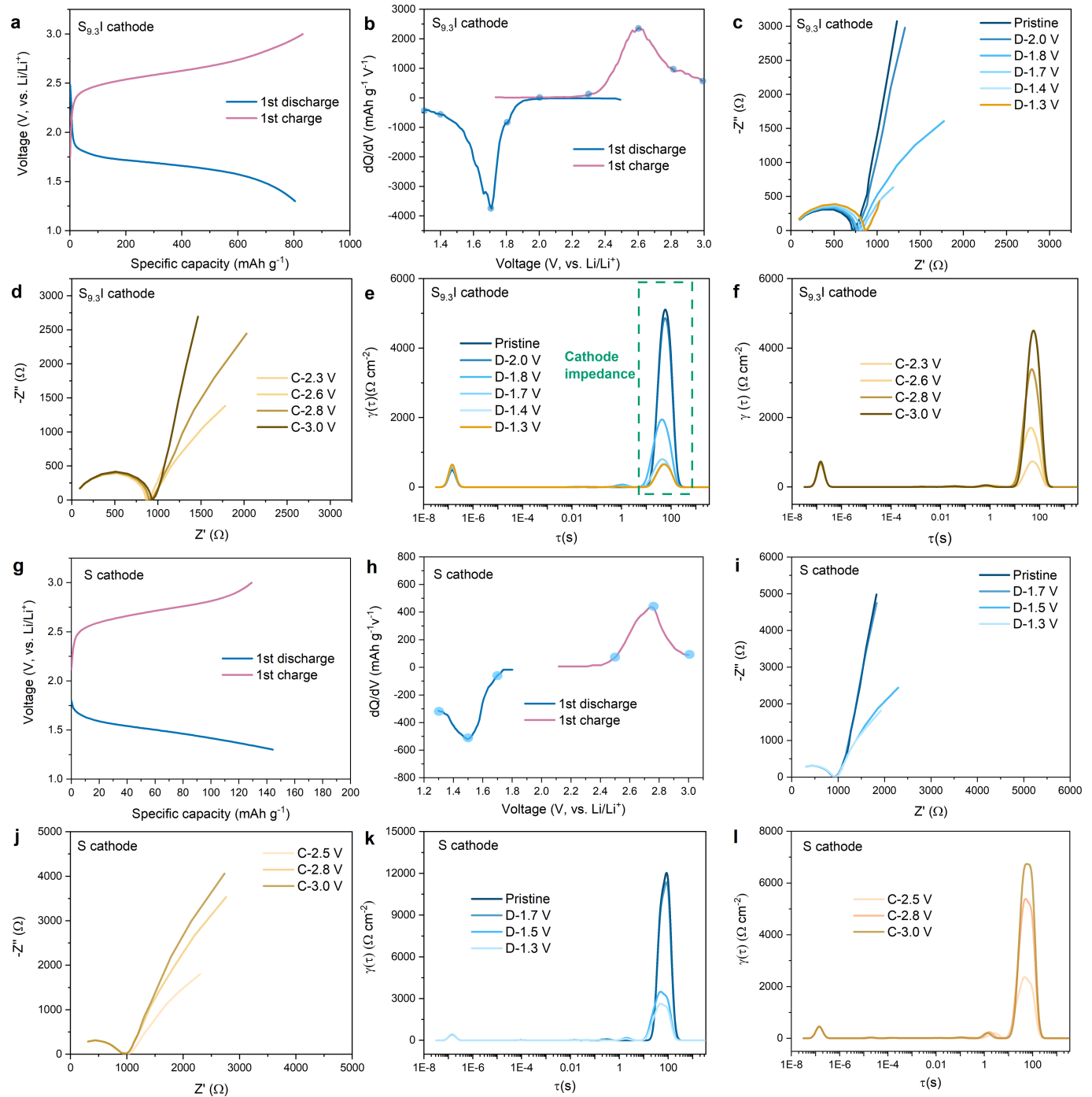
symbols represent Li metal anode based SSLSBs while other cells used non-Li metal anodes. (h) The cycling performance of S<sub>9.3</sub>I cathode with a high mass loading of 4.2 mg cm<sup>-2</sup> at 0.32 A g<sup>-1</sup> and at 100 °C. (i) The corresponding voltage profiles at different cycles in (h). (j) Cycling stability comparison between Li-S<sub>9.3</sub>I solid state batteries with other reported SSLSBs. The cycling performance of the S<sub>9.3</sub>I cathode at varied temperatures and current densities: (k) 80 °C, 0.8 A g<sup>-1</sup>, (l) 60 °C, 0.8 A g<sup>-1</sup>, (m) 40 °C, 0.32 A g<sup>-1</sup>. It should be noted that a low current density was applied to the cells tested at all temperatures during the initial formation cycle.



**Extended Data Fig. 7 | Morphological study of the Li-SP-LPSCI interface during cycling in full cells.** The cross-sectional SEM of Li/SP/LPSCI interface at different states: pristine (a), fully discharged to 1.5 V (b) and fully charged back to 3.0 V (c). It should be noted that all of the anode interfaces were cut from the full cells with the configuration of S<sub>9.3</sub>I-LPS-VGCF/LPS/LPSCI/SP/Li with a high mass loading of S<sub>9.3</sub>I 4.2 mg cm<sup>-2</sup> running at 100 °C and at a current density of 0.32 A g<sup>-1</sup>. At the pristine state (a), both the Li/SP interface and SP/LPSCI SE

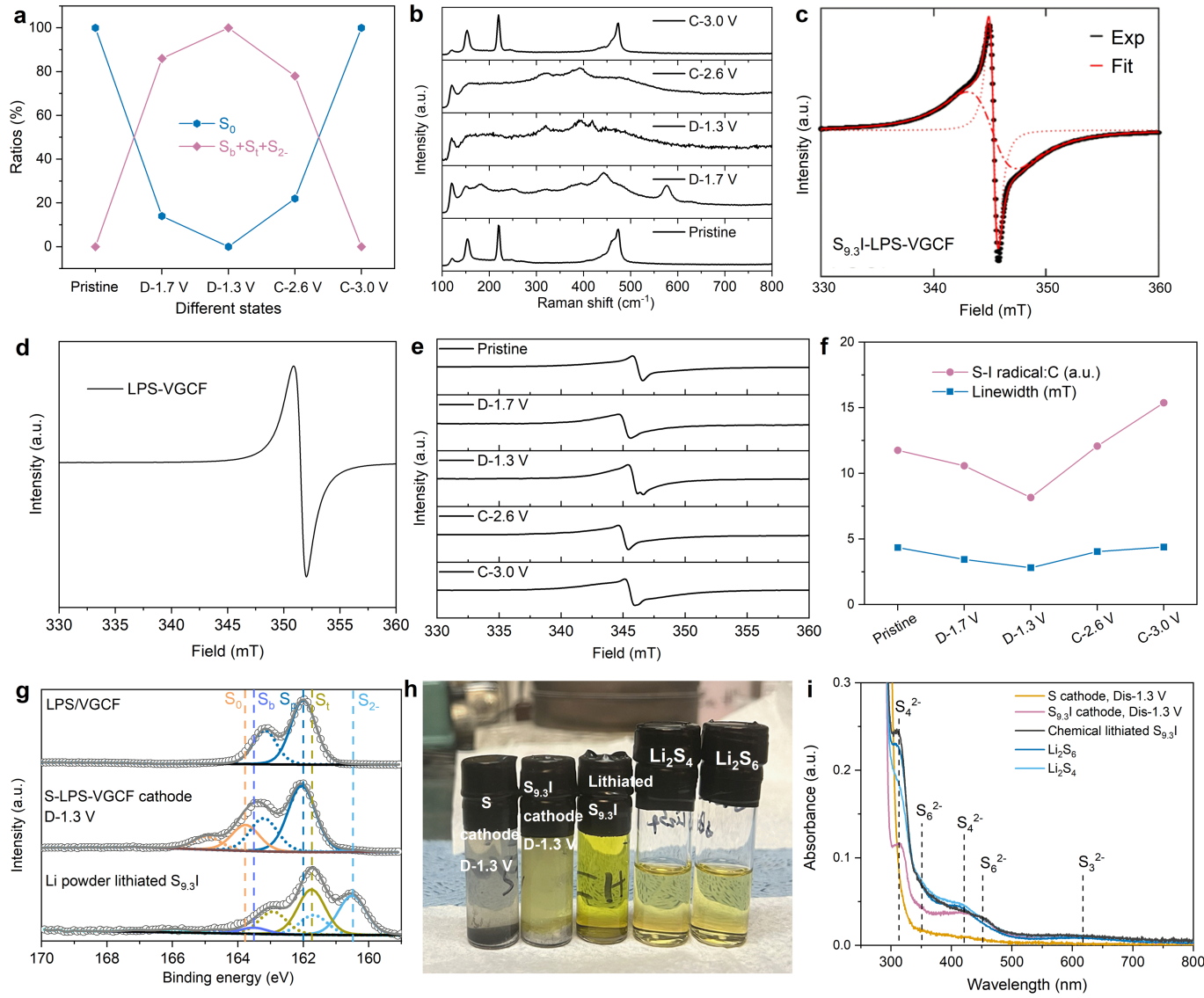
interface are well connected. After discharge (b), the thickness of Li decreases from ~50 μm to ~30 μm, the 20 μm difference corresponding to an area capacity of ~4.0 mAh cm<sup>-2</sup>. After charging back to 3.0 V (c), the thickness of Li recovers back to ~50 μm. Importantly, both the Li/SP interface and SP/LPSCI SE interface are well maintained without the growth of Li dendrites during the discharge and charge processes.

# Article



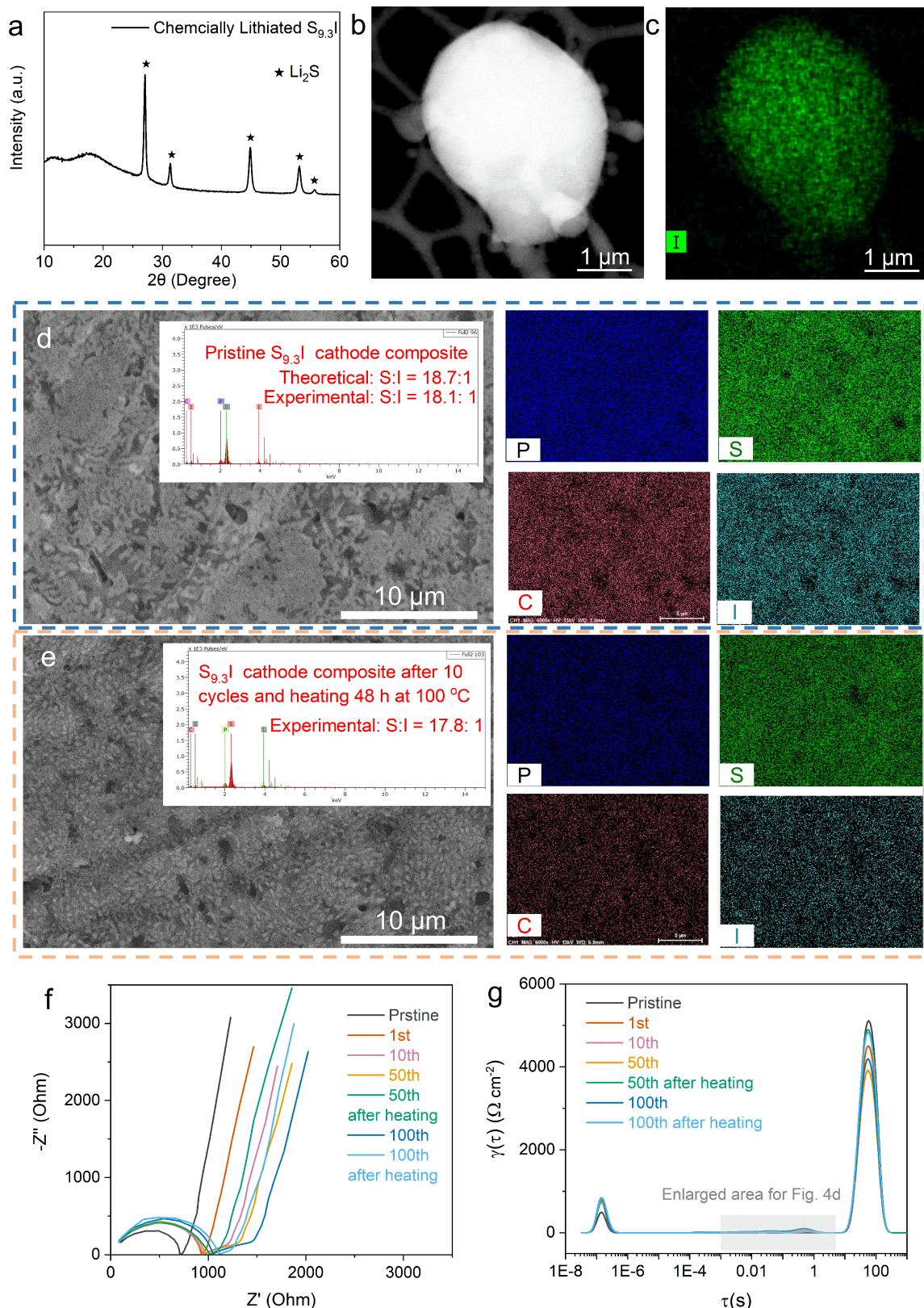
**Extended Data Fig. 8 | EIS study of Li-S<sub>9.3</sub>I and Li-S full cell at 25 °C during initial cycles.** (a) The initial discharge/charge curves of a Li-S<sub>9.3</sub>I cell, and the corresponding dQ/dV curves (b) derive from (a). (c) The EIS of the Li-S<sub>9.3</sub>I cell at different states of discharge. (d) The EIS of the Li-S<sub>9.3</sub>I cell at different states of charge. The DRT analysis of EIS at different states of discharge (e) related to (c), and states of charge (f) related to (d). (g) The initial discharge/charge curves of

a Li-S cathode, and the corresponding dQ/dV curves (h) derive from (g). (i) The EIS of the Li-S cell at different states of discharge. (j) The EIS of the Li-S cell at different states of charge. The DRT analysis of EIS at different states of discharge (k) related to (i), and states of charge (l) related to (j). The impedance of S<sub>9.3</sub>I cathode is much lower than that of pure S cathode during cycling.



**Extended Data Fig. 9 | Characterizations of intermediates during cycling to diagnose the  $S_{9.3}\text{I}$  cathode working mechanism.** (a) The corresponding ratios of  $S_0$ ,  $S_b$ ,  $S_i$ , and  $S_{2^-}$  in the  $S_{9.3}\text{I}$  cathode in Fig. 3b at different discharge/charge states. (b) Ex situ Raman spectra of  $S_{9.3}\text{I}$  during the discharge/charge processes. The ex situ Raman spectra suggest the good reversibility of  $S_{9.3}\text{I}$  cathode at RT. X-band EPR spectra obtained on (c) the pristine  $S_{9.3}\text{I}$  cathode, and on (d) the SSE and carbon mixture (LPS-VGCF). (e) Ex situ EPR data obtained on cathode samples harvested from cells stopped at various stages of the initial discharge/charge processes. (f) Parameters obtained from fits of the EPR spectra in (e), including the ratios of the signal intensities from the  $S_{9.3}\text{I}$  cathode material and from the VGCF additive, and the linewidth of the  $S_{9.3}\text{I}$  EPR signal. The ratio of  $S_{9.3}\text{I}$  radicals to carbon decreases during initial discharge and grows upon subsequent charge (f). This trend is consistent with the following model,

assuming that polysulfide chains that form in the solid-state exist as dianions and cannot be detected in our EPR measurements, unlike EPR-active polysulfide radicals formed in solution through disproportionation of polysulfide dianions (as in conventional Li-S cells). (g) The  $S_{2p}$  high resolution XPS of comparison samples, including LPS/VGCF mixture, S cathode discharge to 1.3 V (D-1.3 V) and chemically lithiated  $S_{9.3}\text{I}$  prepared by reacting with Li powder with an equivalent capacity of ~800 mAh g<sup>-1</sup>. (h) Digital photos of elemental S cathode discharged to 1.3 V,  $S_{9.3}\text{I}$  cathode discharged to 1.3 V, chemically lithiated  $S_{9.3}\text{I}$  immersed in THF solution and standard  $\text{Li}_2\text{S}_4$ ,  $\text{Li}_2\text{S}_6$  THF solutions. (i) The UV-Vis spectra of corresponding samples in (h). The  $S_{9.3}\text{I}$  cathode discharged to 1.3 V and chemically lithiated  $S_{9.3}\text{I}$  suspensions exhibit the color of  $\text{LiS}_x$  solutions immediately, but elemental S cathode discharged to 1.3 V doesn't show any change.



**Extended Data Fig. 10 | Structure and property evolution of  $S_{9.3}I$  cathode during cycling.** (a) XRD of chemically lithiated  $S_{9.3}I$ . A chemically lithiated  $S_{9.3}I$  particle with a few micrometers (b) and corresponding iodine element mapping (c) shows a uniform iodine distribution. EDX mapping images of  $S_{9.3}I$  cathode at different states: (d) Pristine, (e) after 10 cycles and heated over 48 h

at 100 °C, and the corresponding element analysis. There is only a very small S:I atomic ratio change after 10 cycles and then heated at 100 °C for over 48 h, indicating the thermal stability of  $S_{9.3}I$  cathode. (f) EIS spectra and (g) corresponding DRT analysis of Li- $S_{9.3}I$  full cell at different cycles.

**Extended Data Table 1 | Comparison of experimental bulk S<sub>8</sub> cell parameters with PBE, optB88 and SCAN computed values**

Cell parameter	Experimental	PBE	Optb88	SCAN
a (Å)	10.474	11.528 (10.06%)	10.333 (-1.34%)	10.587 (1.08%)
b (Å)	12.881	13.802 (7.15%)	12.829 (-0.40%)	12.952 (0.552%)
c (Å)	24.491	25.822 (5.43%)	24.509 (0.048%)	24.567 (0.313%)

The percentage errors with respect to experimental value are provided in parentheses.

# Article

**Extended Data Table 2 | Comparison of cycling stability and rate capacities of S<sub>9.3</sub>I and other previously reported high performance S composites cathodes in SSLSBs**

S composite active material	S ratio, wt%	SSE	Anode	Cycling stability	Capacity based on S at varied current densities	Capacity based on S composite at varied current densities
S@CNTs <sup>9</sup>	70	LGPS	Li-Al alloy	100 cycles, 86.79%	1362, 1239, 1110, 914, and 514 mAh g <sup>-1</sup> at 0.17, 0.33, 0.5, 0.84, and 1.67 A g <sup>-1</sup>	953.4, 867.3, 777, 639.8, 359.8 mAh g <sup>-1</sup> at 0.12, 0.23, 0.35, 0.59 and 1.17 A g <sup>-1</sup>
S@C <sup>13</sup>	60	LPSC-I	Li-Mg-Li <sub>5</sub> B <sub>4</sub> -AgC alloy	60 cycles, 82%	1530, 1300, 1280, 1180, 1042 mAh g <sup>-1</sup> at 0.16, 0.32, 0.48, 0.64, and 0.8 A g <sup>-1</sup>	918, 780, 768, 708, 625.2 mAh g <sup>-1</sup> at 0.1, 0.19, 0.29, 0.38, and 0.48 A g <sup>-1</sup>
rGO@S <sup>14</sup>	40	LGPS	Li	93.5%, 30 cycles, 0.8 A g <sup>-1</sup>	1525.6, 1384.5, 1336.3, 903.2, 502.6, and 204.7 mAh g <sup>-1</sup> at 0.08, 0.16, 0.83, 1.67, 3.34, and 8.37 A g <sup>-1</sup>	610.2, 553.8, 534.5, 361.3, 201, 81.9 at 0.03, 0.07, 0.33, 0.67, 1.34, 3.35 A g <sup>-1</sup>
SPAN <sup>22</sup>	40	PVDF-HFP-in-LiFSI	Li-In alloy	100 cycles, 67.7%	1306.8, 1189.3, 1078.6, and 928.8 at 0.16, 0.32, 0.83, and 1.6 A g <sup>-1</sup>	522.7, 475.7, 431.4, 371.5 mAh g <sup>-1</sup> at 0.06, 0.13, 0.33, and 0.64 A g <sup>-1</sup>
S <sup>23</sup>	100	LiDFT FSI/PEO	Li	72.6% at 100 <sup>th</sup> cycle, 58.1% at 200 <sup>th</sup> cycle, 40.3% at 400 <sup>th</sup> cycle	930, 620, 380, 220 mAh g <sup>-1</sup> at 0.08, 0.16, 0.32, and 0.8 A g <sup>-1</sup>	930, 620, 380, 220 mAh g <sup>-1</sup> at 0.08, 0.16, 0.32 and 0.8 A g <sup>-1</sup>
Se <sub>0.05</sub> S <sub>0.95</sub> @pPAN <sup>24</sup>	66	LGPS	Li-In alloy	150 cycles, 81.6%, 0.16 A g <sup>-1</sup>	842.2, 742.9, 555.7 and 434.6 mAh g <sup>-1</sup> at 0.16, 0.32, 0.8 and 1.6 A g <sup>-1</sup>	555.8, 490.3, 366.8 and 286.8 mAh g <sup>-1</sup> at 0.11, 0.21, 0.53, and 1.1 A g <sup>-1</sup>
SeS <sub>2</sub> <sup>25</sup>	44	LGPS	Li	50 cycles, 89.2%, 0.05 A g <sup>-1</sup>	1450, 1329.5, 1282.7, and 1144.3 mAh g <sup>-1</sup> at 0.44, 0.89, 1.33, and 2.23 A g <sup>-1</sup>	1024, 970, 949, and 887 mAh g <sup>-1</sup> at 0.2, 0.4, 0.6, and 1 A g <sup>-1</sup>
S/PAN <sup>26</sup>	44	LCE	Li	50 cycles, 33.2%, 0.16 A g <sup>-1</sup>	1183, 719, and 482 mAh g <sup>-1</sup> at 0.32, 0.8, and 1.6 A g <sup>-1</sup>	520.5, 316.4, 212.1 mAh g <sup>-1</sup> at 0.14, 0.35, and 0.7 A g <sup>-1</sup>
S <sup>27</sup>	100	LPB	Li-In alloy	400 cycles, 89.9%, 0.16 A g <sup>-1</sup>	1144.6, 1024.0, 907.8, and 663.0 mAh g <sup>-1</sup> at 0.16, 0.5, 0.83 and 1.675 A g <sup>-1</sup>	1144.6, 1024.0, 907.8, and 663.0 mAh g <sup>-1</sup> at 0.16, 0.5, 0.83 and 1.675 A g <sup>-1</sup>
Li <sub>2</sub> S@Co-C@MHF <sup>28</sup>	65	SPE	Si@MHF	86%, 300 cycles, 0.23 A g <sup>-1</sup>	760, 650, 590, 520 mAh g <sup>-1</sup> at 0.23, 0.58, 1.16, and 2.33 A g <sup>-1</sup>	494, 422, 383, 338 mAh g <sup>-1</sup> at 0.15, 0.38, 0.75, and 1.51 A g <sup>-1</sup>
S <sub>9.3</sub> I, Our work	70	LPS/L PSCI	Li	98.3% 50 <sup>th</sup> cycle, 96.9% 100 <sup>th</sup> cycle, 96.1% 200 <sup>th</sup> , 91.4% 300 <sup>th</sup> , 87% 400 <sup>th</sup> , 0.16 A g <sup>-1</sup>	1655.3, 1467.1, 1354.4, 1309, 1252.7, 1211.4, 1147.1, 1070, 978.3, 891.4, 699.1 at 0.23, 0.46, 0.68, 1.14, 1.83, 2.28, 3.43, 4.57, 5.71, 6.86 and 8.0 A g <sup>-1</sup>	1158.7, 1027, 948.1, 916.3, 876.9, 848, 803, 749, 684.8, 624, 489.4 at 0.16, 0.32, 0.48, 0.80, 1.28, 1.60, 2.40, 3.20, 4.00, 4.80 and 5.60 A g <sup>-1</sup>

The comparison includes rate performance based on S only/S cathode composites and long term cycling stability of our S<sub>9.3</sub>I cathode and previously reported S cathodes<sup>9,13,14,22-28</sup>.